

Reassessing the Effect of Cloud Type on Earth's Energy Balance in the Age of Active Spaceborne Observations. Part I: Top of Atmosphere and Surface

TRISTAN S. L'ECUYER AND YUN HANG

Department of Atmospheric and Oceanic Sciences, University of Wisconsin–Madison, Madison, Wisconsin

ALEXANDER V. MATUS

Space Science and Engineering Center, University of Wisconsin–Madison, Madison, Wisconsin

ZHIEN WANG

Department of Atmospheric and Oceanic Sciences and Laboratory for Atmospheric and Space Physics, University of Colorado Boulder, Boulder, Colorado

(Manuscript received 2 November 2018, in final form 8 April 2019)

ABSTRACT

This study revisits the classical problem of quantifying the radiative effects of unique cloud types in the era of spaceborne active observations. The radiative effects of nine cloud types, distinguished based on their vertical structure defined by *CloudSat* and *CALIPSO* observations, are assessed at both the top of the atmosphere and the surface. The contributions from single- and multilayered clouds are explicitly diagnosed. The global, annual mean net cloud radiative effect at the top of the atmosphere is found to be $-17.1 \pm 4.2 \text{ W m}^{-2}$ owing to $-44.2 \pm 2 \text{ W m}^{-2}$ of shortwave cooling and $27.1 \pm 3.7 \text{ W m}^{-2}$ of longwave heating. Leveraging explicit cloud base and vertical structure information, we further estimate the annual mean net cloud radiative effect at the surface to be $-24.8 \pm 8.7 \text{ W m}^{-2}$ ($-51.1 \pm 7.8 \text{ W m}^{-2}$ in the shortwave and $26.3 \pm 3.8 \text{ W m}^{-2}$ in the longwave). Multilayered clouds are found to exert the strongest influence on the top-of-atmosphere energy balance. However, a strong asymmetry in net cloud radiative cooling between the hemispheres (8.6 W m^{-2}) is dominated by enhanced cooling from stratocumulus over the southern oceans. It is found that there is no corresponding asymmetry at the surface owing to enhanced longwave emission by southern ocean clouds in winter, which offsets a substantial fraction of their impact on solar absorption in summer. Thus the asymmetry in cloud radiative effects is entirely realized as an atmosphere heating imbalance between the hemispheres.

1. Introduction

Earth's climate is strongly regulated by the spatial and temporal variability of clouds. Variations in cloud phase, height, thickness, and vertical structure all modulate the way clouds influence the propagation of solar and thermal radiation through the atmosphere. Accurately modeling the sensitivity of climate to external forcing, therefore, requires a precise accounting of the radiative feedbacks owing to cloud changes. Yet it is not sufficient to merely tune models to represent the global net cloud effects since feedbacks depend critically on cloud characteristics, their location, and their environment (Stephens 2005; Bony et al. 2006) and thus models must correctly represent

radiative effects of distinct cloud types, their spatial distributions, and their temporal variability instead of relying on tuning the global-mean radiative energy to be balanced for the present-day climate. However, uncertainty remains concerning how different cloud types regulate radiative fluxes on global scales, which impedes progress toward constraining the processes that govern spatial and temporal variability in cloud radiative effects. This is related to the fact that global models continue to exhibit significant cloud biases, such as insufficient boundary layer clouds and a poor representation of multilayered cloud systems, that may significantly impact their ability to simulate cloud feedbacks (Zhang et al. 2005; Su et al. 2010, 2013; Bodas-Salcedo et al. 2014; Calisto et al. 2014).

Classifying cloudy scenes in observations has been the subject of vigorous research for more than two centuries

Corresponding author: Yun Hang, yhang4@wisc.edu

DOI: 10.1175/JCLI-D-18-0753.1

© 2019 American Meteorological Society. For information regarding reuse of this content and general copyright information, consult the [AMS Copyright Policy \(www.ametsoc.org/PUBSReuseLicenses\)](https://www.ametsoc.org/PUBSReuseLicenses).

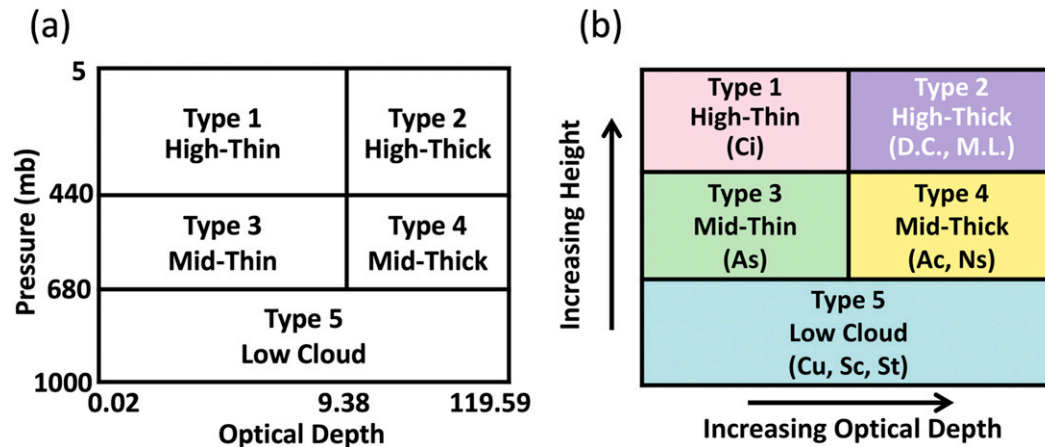


FIG. 1. (a) Five classes of cloud defined according to the ISCCP radiance classification (Hartmann et al. 1992), and (b) equivalent classification based on true cloud height and cloud thickness according to the *CloudSat* and *CALIPSO* 2BCLD.

(Howard 1803, 1843). In situ and ground-based cloud measurements provide high-quality observations at specific locations, but lack global coverage compared to satellites (Kiehl 1994; Hahn and Warren 1999; Wang and Sassen 2001; Comstock et al. 2002; Ackerman and Stokes 2003). Also, ground-based active sensors may miss some high clouds due to attenuation (lidar) or loss of sensitivity (radar) (Protat et al. 2014). Satellite-based cloud detection from passive instruments combined with radiation budget instruments like the Earth Radiation Budget Experiment (ERBE) vastly improved our understanding of cloud distributions and their global radiative impacts (Ramanathan et al. 1989; Harrison et al. 1990; Rossow and Lacis 1990; Wielicki et al. 1996; Rossow and Schiffer 1999). Accurate discrimination of multilayered clouds and precise delineation of cloud top and cloud base attitudes have, however, been challenging in conventional passive sensor approaches given their limited ability to measure cloud vertical structure (Mace et al. 2009; Mace and Wrenn 2013).

Among the early studies to document the radiative properties of distinct cloud types from spaceborne passive observations were those of Ockert-Bell and Hartmann (1992) and Hartmann et al. (1992), who used C1 cloud data from the International Satellite Cloud Climatology Project (ISCCP) (Rossow and Schiffer 1999) and radiative fluxes data from ERBE (Hartmann et al. 1992). The ISCCP C1 product classified clouds into five types (see Fig. 1) according to observed cloud height and optical depth. (Ockert-Bell and Hartmann 1992) and Hartmann et al. (1992) documented the impact of each of these types on top-of-atmosphere longwave and shortwave radiation contrasting the effects of low, midlevel, and high clouds around the globe. The results

provided valuable insights into the factors that govern the distributions of cloud radiative effects and their seasonal variation and served as important benchmarks for evaluating the global models at that time but they were, of course, subject to some limitations. The passive sensors and methods used lacked information for discriminating cloud types at night or distinguishing overlapping cloud fields (Rossow et al. 1985; Chen et al. 2000). Also, the lack of information concerning cloud vertical structure introduces large uncertainties when estimating cloud influences on surface radiation.

Building on these ERBE measurements, the Clouds and the Earth's Radiant Energy System (CERES) instruments on board the Tropical Rainfall Measurement Mission (TRMM), *Terra*, and *Aqua* satellites have significantly improved radiative flux data (Wielicki et al. 1996). The ISCCP D1 cloud product coupled new cloud retrieval methods to radiative transfer models to further estimate the radiative impacts of cloud types at the surface (SFC) (Chen et al. 2000). Likewise, the CERES Surface Radiation Budget (SRB) product has been developed to derive the shortwave and longwave surface radiative fluxes on a global scale (Gupta et al. 1999). These datasets have been extensively validated against surface flux observations from the Baseline Surface Radiation Network (BSRN) to ensure that they yield accurate estimates of downwelling longwave and shortwave fluxes on monthly scales (Zhang et al. 2013). However, the limited information concerning cloud base or the presence of multiple cloud layers in the passive observations used by both ISCCP and SRB continues to hamper our ability to quantifying the radiative impacts of some complex cloud types (Rossow and Zhang 1995;

Zhang et al. 1995; Gupta et al. 1999; Zhang et al. 2005; Loeb et al. 2009; Wild et al. 2013).

Our understanding of the influence of distinct cloud types on Earth's radiation budget continues to be advanced with new definitions of ISCCP cloud-based weather states (e.g., Jakob and Tselioudis 2003; Oreopoulos and Rossow 2011). Another approach called "cloud object analysis" categorizes similar satellite footprints in a contiguous region to examine the influence of cloud regimes on radiative budget (Xu et al. 2005; Bacmeister and Stephens 2011; Xu et al. 2016). Also, Moderate Resolution Imaging Spectroradiometer (MODIS) (Platnick et al. 2003) cloud types have been updated using the latest cloud retrievals (Oreopoulos et al. 2016). While these studies continue to provide significant insights into the role distinct cloud types play in defining Earth's radiation budget, new profiling capabilities afforded by spaceborne active sensors offer potential for refining the analysis to include explicit cloud boundary information not available through conventional means (Stephens et al. 2018). It is the goal of this paper to revisit the role of distinct cloud types in Earth's energy budget within the context of the new vertical dimension provided by *CloudSat* and *CALIPSO*.

Since 2006, the active sensors aboard *CloudSat* and *Cloud-Aerosol Lidar and Infrared Pathfinder Satellite Observations* (*CALIPSO*) have provided detailed near-global observations of cloud vertical structures (Stephens et al. 2002). This information is concisely summarized in *CloudSat*'s level 2 cloud scenario classification (2B-CLDCLASS-lidar, hereafter 2BCLD) product (Sassen and Wang 2012) that combines radar and lidar measurements to distinguish canonical cloud types based on explicitly constrained cloud boundaries, two-dimensional cloud structure, cloud phase, and precipitation features through a neural network approach. *CloudSat*'s level 2 radiative flux and heating rate (2B-FLXHR-lidar, hereafter 2BFLX) algorithm combines this information with cloud properties and scene characteristics from *CloudSat*, *CALIPSO*, and MODIS to compute vertical profiles of shortwave (SW) and longwave (LW) radiative fluxes for each *CloudSat* field of view. Together the 2BCLD and 2BFLX datasets provide the basis needed to reassess the effect of cloud type on Earth's energy balance in the modern satellite era.

This paper is organized as follows. In section 2, we briefly describe each dataset and the methods used in this analysis. In section 3, we will discuss global distribution of radiative effect by individual cloud type at the TOA. After that, we will document how these state-of-the-art sensors offer the required advances in cloud boundary information to discern the radiation at the surface. Finally, a summary and discussion will be given

in section 4. A subsequent study (Hang et al. 2019) will examine the implications of cloud type for radiative heating and cooling within the atmosphere.

2. Datasets

a. *CloudSat's 2B-CLDCLASS-lidar data product*

While classifying clouds by their pressure and optical depth has led to important breakthroughs in our understanding of cloud feedbacks, active sensors offer potential for further refining constraints on cloud vertical structure (L'Ecuyer and Jiang 2010). *CloudSat*'s 2BCLD product utilizes collocated *CloudSat*, *CALIPSO*, and MODIS measurements to explicitly incorporate two-dimensional cloud characteristics into a vertical and spatial structure-based cloud classification scheme (Sassen et al. 2008; Sassen and Wang 2012). *CloudSat*'s 94-GHz nadir-looking Cloud Profiling Radar (CPR) has a minimum sensitivity of approximately -30 dBZ (at launch and for the time period considered here). The radar cross-track resolution is approximately 1.4×1.7 km² and with a vertical resolution of 480 m, which is further oversampled to 240 m (Tanelli et al. 2008). Since *CloudSat*'s CPR is relatively less sensitive to small particles, the Cloud-Aerosol Lidar with Orthogonal Polarization (CALIOP) on board *CALIPSO* provides complementary measurements of subvisual cirrus and low-lying liquid clouds that go undetected by the CPR (McGill et al. 2007; Winker et al. 2007; Henderson et al. 2013). Together, these sensors provide the most accurate depiction of the vertical distribution of clouds currently available (Mace et al. 2009). Furthermore, combined CPR and CALIOP measurements provide reliable cloud phase (liquid, ice, or mixed phase) discrimination for each cloud layer (Zhang et al. 2010). In addition, MODIS provides complementary measurements of cloud effective radius and integrated optical thickness that further constrain cloud radiative properties (Platnick et al. 2003; Ackerman et al. 2008; Chan and Comiso 2011).

Compared to ISCCP and other similar cloud type schemes, the *CloudSat* 2BCLD product not only provides information for cloud type characterization more faithfully but also helps fill gaps in understanding multilayered clouds. The 2BCLD product groups cloud scenes into different layers, then classifies cloud clusters into stratus (St), stratocumulus (Sc), cumulus (Cu) (including Cu congestus), nimbostratus (Ns), altocumulus (Ac), altostratus (As), deep convective clouds (D.C.), or high clouds (cirrus and cirrostratus) based on cloud height and phase, maximum effective radar reflectivity factor, and temperature, as well as the presence of

precipitation reaching the surface. For boundary layer clouds, St and Sc are mainly separated by horizontal homogeneity based on cloud-top height and radar reflectivity. Cu includes fair weather cumulus and deep cumulus congestus. Fair weather cumulus clouds are separated from St and Sc with cloud fraction. Specific definitions for each cloud category can be found in [Sassen and Wang \(2008\)](#). If more than one cloud type is identified in multiple distinct cloud layers separated by at least one CPR vertical range bin, then that pixel is classified as a multilayered (M.L.) cloud. Note that this definition of M.L. cloud is not limited to multilayered clouds consisting of distinct liquid and ice layers ([Matus and L'Ecuyer 2017](#)), but also includes mixed phase clouds. Together, *CloudSat* and *CALIPSO* likely observe the majority of all multilayered clouds with one exception. They can miss very low clouds that lie below optically thick overlying high or mixed-phase clouds where the lidar attenuates in the upper cloud and the radar misses the lower cloud layer due to ground clutter ([Protat et al. 2014](#)). In this case, the missing clouds have negligible impact on TOA cloud forcing and weak impact on surface LW cloud forcing. Other missing clouds from combined *CloudSat* and *CALIPSO* do happen, but at a relatively low frequency. With the low occurrence, we do not expect the missing clouds to noticeably impact the statistical results reported.

b. *CloudSat's 2B-FLXHR-lidar data product*

The *CloudSat* 2BFLX algorithm derives estimates of broadband fluxes consistent with retrievals of atmospheric, cloud, and surface properties from *CloudSat*, *CALIPSO*, and MODIS ([L'Ecuyer et al. 2008](#)). This study uses the fifth release (R05) of the 2BFLX dataset that features improvements in mixed-phase and ice cloud properties ([Matus and L'Ecuyer 2017](#)). Compared with the previous version (R04) of 2BFLX ([Henderson et al. 2013](#)), the R05 implements ice cloud properties from *CloudSat* 2C-ICE product, which provides more rigorous treatment of thin ice clouds that includes explicit retrievals of ice water content (IWC) and effective radii ([Deng et al. 2013](#); [Ham et al. 2017](#); [Matus and L'Ecuyer 2017](#)). The R05 2BFLX product remains sensitive to retrieval errors and sampling biases introduced by the limited spatial and temporal sampling characteristics of *CloudSat* and *CALIPSO*, especially on the scale of individual cloud system. Nevertheless, the algorithm has been demonstrated to provide a robust statistical representation of CERES top of the atmosphere fluxes when integrated over monthly and longer scales. The CERES instrument aboard *Aqua* provides a unique opportunity for evaluating 2BFLX because of the small temporal gap

between the orbits of the *Aqua* satellite and *CloudSat* ([Kato et al. 2010](#)).

While the vertical structure information provided by spaceborne active sensors provides significant new insights into the role of distinct cloud types in the global energy budget, these data are not without their limitations. The spatial and temporal characteristics of *CloudSat* and *CALIPSO* may introduce sampling biases in the results. For example, the diurnal variations in cloud cover are not properly accounted for by the limited twice-daily sampling of the A-Train. Also, these datasets do not provide full global coverage, omitting regions of 82.5°–90°. Uncertainties may also be present in the radiative effects estimated from 2B-FLXHR-lidar owing to cloud detection and cloud microphysical property retrievals. Liquid water content, surface temperature, and lower-troposphere humidity, in particular, exert strong influences on surface flux estimates that drive the error bars presented here ([Henderson et al. 2013](#)). In addition, [Mülmenstädt et al. \(2018\)](#) recently reported that significant regional errors may exist in downwelling LW fluxes due to uncertainty in cloud base heights. All uncertainty estimates reported in this study derive from the comparisons found in [Matus and L'Ecuyer \(2017\)](#) and a comprehensive set of sensitivity studies is reported in [Henderson et al. \(2013\)](#). Additional details concerning 2BFLX performance can be found in those studies.

An example profile from R05 2BFLX is shown in [Fig. 2](#), which shows the reflectivity and cloud mask as well as the corresponding cloud radiative effects (CREs) estimated from 2BFLX at the TOA and SFC. According to 2BCLD, clouds are categorized as cirrus, altostratus, and multilayered clouds. The multilayered clouds cases have strong SW effects that dominate net CRE while the altostratus-only portion shows small net CRE.

c. *Methodology*

This study documents the radiative effects of nine vertical structure-based cloud types on radiant energy balance. The analysis uses data from the pre-anomaly phase of the *CloudSat* mission from January 2007 to December 2010 and covers the complete, near-global sampling provided by *CloudSat* and *CALIPSO* from 82.5°S to 82.5°N. All data are gridded to $2.5^\circ \times 2.5^\circ$ spatial resolution to ensure adequate sampling on monthly time scales. Since *CloudSat* and *CALIPSO* measurements are always collected at 0130 and 1330 local time (LT), the estimated SW fluxes are normalized to the diurnally averaged insolation to approximate the full diurnal cycle. Here this is achieved by multiplying the shortwave fluxes for each *CloudSat* pixel by the diurnally averaged insolation for that day and location.

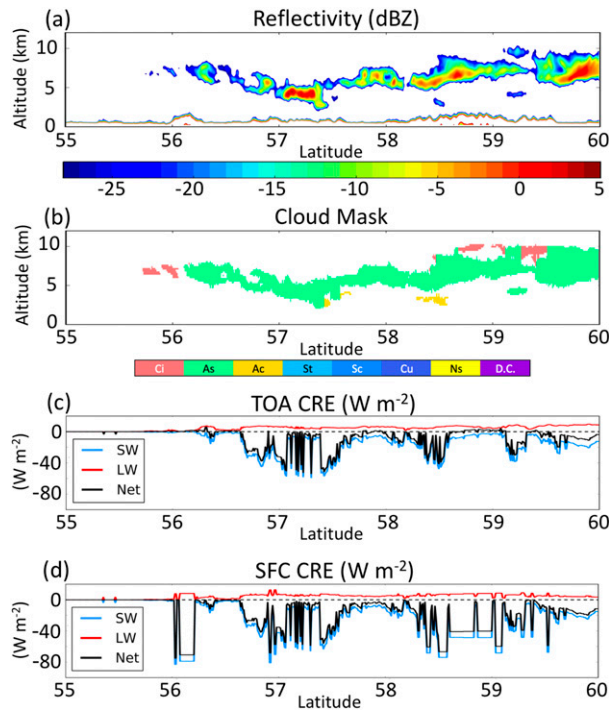


FIG. 2. Selected inputs and outputs of 2BFLX from a portion of granule 05806 between 55° and 60°N. (a) Observed reflectivity and (b) cloud mask, and calculated cloud radiative effect (CRE) at (c) the top of the atmosphere (TOA) and (d) the surface (SFC).

This does not account for diurnal variations in cloud cover other than those directly observed at the two sampling times at 0130 and 1330 LT.

With this limitation in mind, the global annual mean net CRE at the TOA ($C_{\text{Net,TOA}}$) in this dataset is estimated to be $-17.1 \pm 4.2 \text{ W m}^{-2}$, with $-44.2 \pm 2 \text{ W m}^{-2}$

in the shortwave ($C_{\text{SW,TOA}}$) and $27.1 \pm 3.7 \text{ W m}^{-2}$ in the longwave ($C_{\text{LW,TOA}}$) (Matus and L'Ecuyer 2017). The spatial distribution of $C_{\text{Net,TOA}}$ is shown in Fig. 3. Clouds are observed to exert a net cooling effect over much of the global peaking over the midlatitude oceans. Smaller net warming effects are evident over tropical land regions, most notably equatorial Africa, and in polar regions. The resulting net TOA CRE is somewhat weaker than previous estimates from ISCCP (-25 W m^{-2}) (Raschke et al. 2016), possibly due to biases in assigning optical properties in some regions (Zhang et al. 2004; Allan 2011; Stackhouse et al. 2011), but agrees well with the latest estimates from CERES (-17.9 W m^{-2}) (Loeb et al. 2018).

In addition to estimating radiative effects at the TOA, cloud boundary information from *CloudSat* and *CALIPSO* allows surface cloud radiative effects to be estimated more accurately than from passive sensors. In general, SW CRE at the surface is larger than the TOA due to atmospheric absorption. The global annual average net CRE at the surface ($C_{\text{Net,SFC}}$) is estimated to be $-24.8 \pm 8.7 \text{ W m}^{-2}$, with contributions of $-51.1 \pm 7.8 \text{ W m}^{-2}$ in the shortwave ($C_{\text{SW,SFC}}$) and $26.3 \pm 3.8 \text{ W m}^{-2}$ in the longwave ($C_{\text{LW,SFC}}$) (Fig. 3). The uncertainties in the surface fluxes are derived based on the sensitivity studies reported in Henderson et al. (2013). Note that in the Henderson et al. (2013) the uncertainty in cloud base height was assumed to be 240 m but recent work of Mülmenstädt et al. (2018) suggests that 480 m is a more appropriate measure of cloud base error. The uncertainties in surface fluxes due to cloud base height errors reported in Table 6 of Henderson et al. (2013) are, therefore, doubled in this study. These estimates of

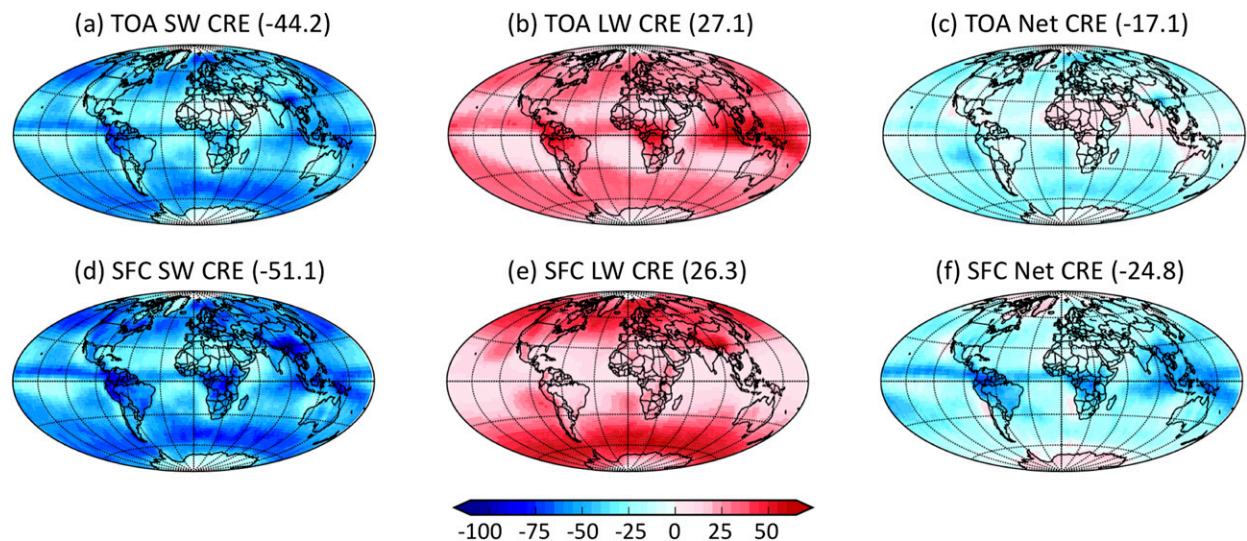


FIG. 3. Annual mean SW, LW, and net cloud radiative effects at the (a)–(c) TOA and (d)–(f) surface (W m^{-2}). All flux data presented are from 2BFLX, 2007–10. The area-weighted global average (in W m^{-2}) is shown in parentheses.

surface cloud radiative effects agree well with derived from Surface Radiation Budget (SRB) dataset (Allan 2011). Compared with previous results from passive sensors, the differences are significant because there is additional complexity involved in computing surface fluxes (in both 2BFLX and CERES) that contributes to additional uncertainty in flux calculations. To estimate surface fluxes based on TOA fluxes, assumptions need to be made regarding cloud base height, trace gases, and aerosols. There are clearly discrepancies in the treatment of these quantities between 2BFLX and CERES. Given the complexity involved, it is fairly challenging to attribute the source of this discrepancy. In fact, the global mean $C_{SW,SFC}$ from SRB (-53 W m^{-2}) is very similar to that reported here. The value of $C_{LW,SFC}$ derived from SRB is somewhat larger (32 W m^{-2}) but still likely within the error bars of both estimates (Stackhouse et al. 2011).

The difference between $C_{Net,TOA}$ and $C_{Net,SFC}$ implies $7.7 \pm 4.5 \text{ W m}^{-2}$ of cloud-induced atmospheric absorption. Note that this atmospheric absorption is defined as the difference between TOA and SFC CRE; as a result, small errors in TOA or SFC can be amplified in atmosphere since it is computed as a difference. This global mean cloud-induced atmospheric heating derives almost entirely from enhanced SW absorption in the presence of clouds (6.9 W m^{-2}). However, unlike the spatial patterns of SW CRE (C_{SW}), which are almost identical at the TOA and SFC, there are substantial differences in the spatial structure of LW CRE (C_{LW}) between the surface and the TOA that demonstrate that clouds exert significant zonal variations in atmospheric heating. Thus SW absorption controls global mean cloud atmospheric heating while strong regional gradients in the strength of cloud LW emission govern its spatial distribution.

3. Radiative effects of cloud types

Figure 4 shows the global distribution of annual mean cloud fraction from *CloudSat* and *CALIPSO* observations, which corresponds to the CRE estimates in Fig. 3. Covering approximately 71% of Earth's surface, clouds are most commonly observed in the intertropical convergence zone (ITCZ) and midlatitude storm tracks, and least frequently over remote subtropical oceans and deserts. A casual comparison of Figs. 3 and 4 clearly demonstrates that total cloud fraction is insufficient for explaining the spatial distribution of net CRE. For example, despite the high net cloud fraction in the ITCZ (80%), $C_{Net,TOA}$ (Fig. 3c) in this region nearly vanishes owing to competing LW and SW radiative effects (Kiehl 1994).

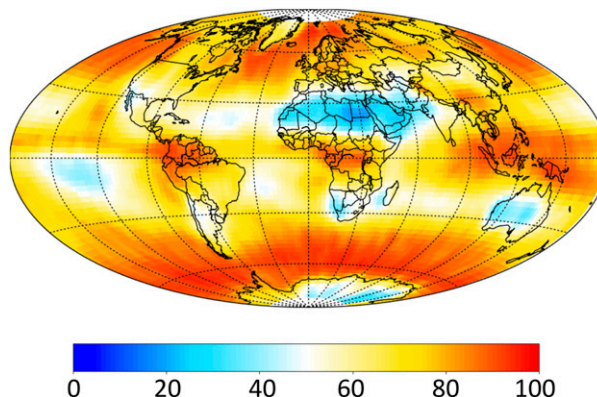


FIG. 4. Annual mean cloud fraction using *CloudSat* and *CALIPSO* observations from 2007 to 2010 (%). The global average is 70.8%.

To understand the distribution of cloud radiative effects, cloudy scenes must be partitioned into distinct regimes. The global distributions of the nine vertical structure-based cloud types identified in the 2BCLD cloud classification are shown in Fig. 5. Here, an explicit distinction is made between pixels containing a single cloud layer and those that contain multiple layers whose radiative characteristics can differ substantially from those of any of the component layers in isolation. Single-layer clouds have further been separated into eight distinct types according to the 2BCLD classification. Note, however, that the more nuanced topic of further discriminating distinct multilayered cloud scenes is left as a subject for future study (Oreopoulos et al. 2017). Instead, we focus on simply distinguishing this complex category of clouds that are often challenging to discriminate using passive sensors. As a result, the frequency and radiative effects of this more diverse category are enhanced relative to their single-layer counterparts but this is done intentionally to illustrate the importance of accurately characterizing such scenes in both observations and models when assessing global cloud radiative effects.

In general, the distributions in Fig. 5 conform to our qualitative understanding of global cloud distributions: high clouds (cirrus, deep convective clouds, and multilayered cloud systems) are most frequently observed near the equator and over tropical continents resulting from the large transport of water vapor into upper levels by persistent convection. Midlevel clouds (altostratus, altocumulus, and nimbostratus clouds) are predominantly observed over storm track regions. Marine boundary layer clouds (stratus, stratocumulus, and cumulus) are prevalent in subsidence regions over midlatitude oceans and subtropical eastern ocean margins. However, Fig. 5 reveals two important distinctions that

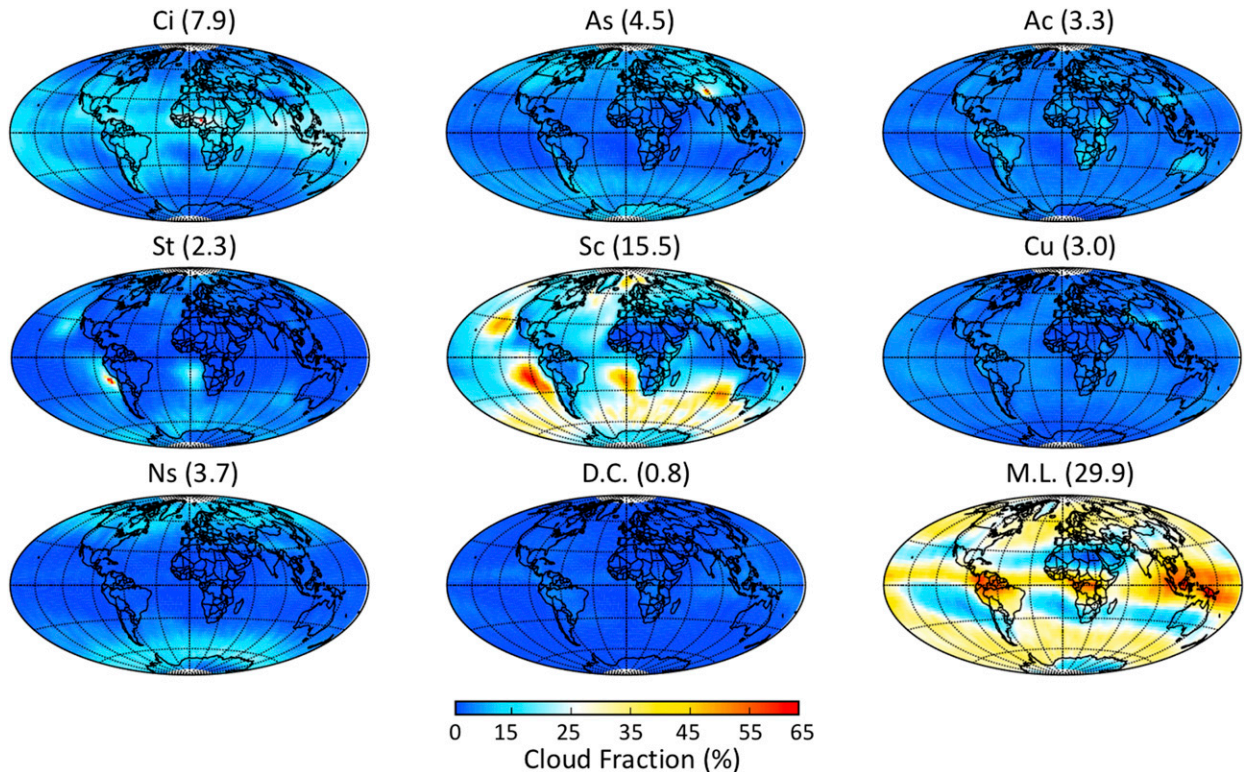


FIG. 5. Breakdown of annual mean cloud fraction (Fig. 4) by cloud type determined based on 2BCLD classification, 2007–10 (%). The area-weighted global average (in %) is shown in parentheses. Ci = cirrus, As = altostratus, Ac = altocumulus, St = stratus, Sc = stratocumulus, Cu = cumulus, Ns = nimbostratus, D.C. = deep convection, and M.L. = multilayered cloud system.

are generally not captured in passive cloud classifications. First, the ability to distinguish single- and multilayered cloud systems reveals that scenes consisting of more than one overlapping cloud layer cover nearly 30% of the globe. By comparison, the fractional coverage of all categories of single-layered cloud combined is 41%, with stratocumulus the most commonly observed single-layer cloud type at 15.5%. Note that the stratocumulus cloud fraction may be overestimated relative to stratus owing to *CloudSat* radar detection limits, which favor larger cloud and drizzle droplets and low cloud horizontal homogeneity (Wang et al. 2012). Second, the ability of active sensors to delineate convective cores at high spatial resolution demonstrates that deep convection represents less than 1% of the cloudy scenes on Earth. From a radiative perspective, it is important to distinguish these convective profiles from the associated cirrus and multilayered clouds even though they may derive from the same storm system in many instances.

a. Top of atmosphere

Cloud radiative effects depend not only on their geographic locations but also on their physical and optical properties (Rossow and Lacis 1990; Hartmann et al.

1992). To quantify this radiative impact at the TOA, the conditional mean CRE of each cloud type i is defined as

$$\langle C_i \rangle = (F_i^\downarrow - F_i^\uparrow)_{\text{all-sky}} - (F_i^\downarrow - F_i^\uparrow)_{\text{clear-sky}}, \quad (1)$$

where F^\downarrow and F^\uparrow are downward and upward fluxes under clear-sky and all-sky conditions in Earth's atmosphere, respectively (Hartmann et al. 1986; Ramanathan et al. 1989; Oreopoulos and Rossow 2011; Henderson et al. 2013). Clear-sky fluxes are obtained through plane-parallel radiative transfer calculations in which all condensed water is removed from the atmosphere, while all-sky fluxes represents the standard 2BFLX calculations described above. The subscript i denotes each of the nine cloud types in 2BCLD product. Each individual C_i is weighted by the global cloud fraction of each cloud type (shown in Fig. 5) to determine its contribution to the total CRE:

$$C_i = \langle C_i \rangle \times CF_i, \quad (2)$$

where $\langle C_i \rangle$ is the conditional mean CRE when cloud type i and CF_i is the corresponding cloud fraction. Figure 6 highlights examples of this calculation for cirrus

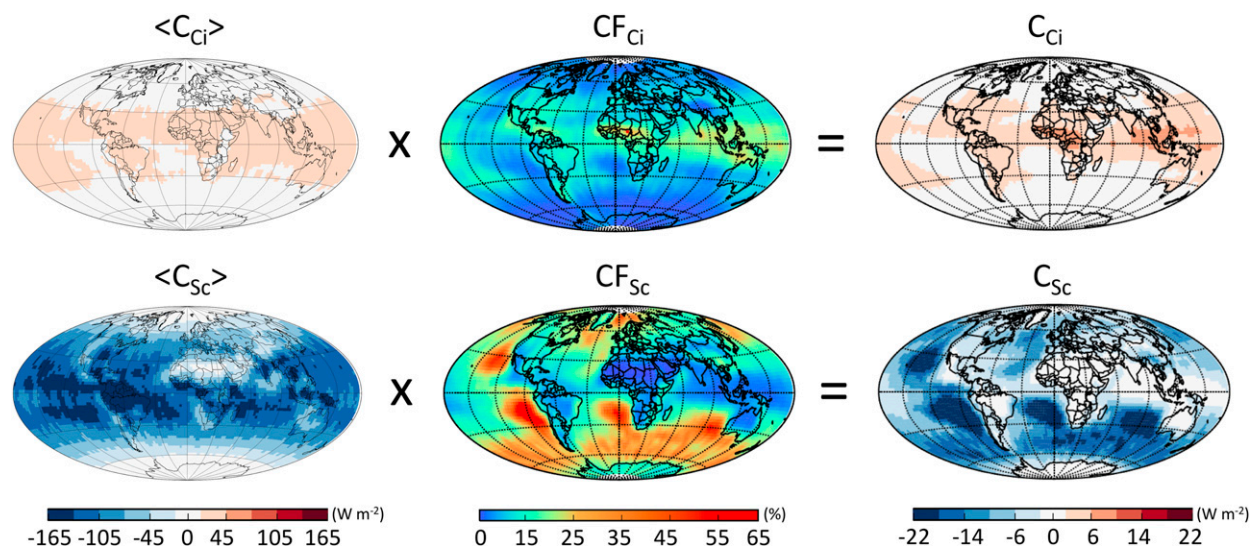


FIG. 6. Selected global maps of $\langle C_i \rangle \times CF_i = C_i$ [for cirrus (Ci) and stratocumulus (Sc) clouds]; $\langle C_i \rangle$ is the total net CRE at TOA when cloud type i is observed, CF_i is the cloud fraction of cloud type i , and C_i shows the contribution of cloud type i to the global CRE.

and stratocumulus clouds. The term C_i shows the contributions of cloud type i to the total CRE, and exhibits more variability than $\langle C_i \rangle$, which only accounts for variation in cloud effects induced by background or environmental conditions and cloud properties. This suggests that, once segregated by type, the spatial distribution of each cloud type plays a bigger role in determining its effect on climate than variations in cloud microphysical structure or environment. However, regional variations in conditional mean CRE are evident such as smaller net C_{Ci} over the Tibetan Plateau, polar regions, and Rocky Mountains where the temperature contrast between cirrus and the colder underlying surfaces is smaller. Figure 6 also reveals that $\langle C_{Sc} \rangle$ is more variable than $\langle C_{Ci} \rangle$ because in the former case there is greater contribution to the net CRE from SW CRE, which is more sensitive to internal cloud property (optical depth) variability within the cloud type, and also depends on systematic variations in solar geometry. The goal of this paper is to contrast the radiative effects of each cloud type in CLDCLASS-lidar, C_i .

1) GLOBAL DISTRIBUTION OF RADIATIVE EFFECT BY INDIVIDUAL CLOUD TYPES

Figures 7–9 display global maps of annual mean $C_{Net,TOA}$, $C_{SW,TOA}$, and $C_{LW,TOA}$ of nine cloud types based on 2BFLX estimates. As shown in Fig. 7, cirrus and stratocumulus clouds exert the strongest net radiative impacts globally of the single-layer cloud types. Cirrus clouds are found to warm the atmosphere and surface by 2 W m^{-2} , on the global annual mean, especially over relatively warm surfaces including the tropical warm

pool and the Sahel region. Stratocumulus clouds, by contrast, exert a large cooling effect of -8.2 W m^{-2} . The most pronounced influences of stratocumulus occur over subtropical oceans where they can exceed -20 W m^{-2} . Altocumulus, stratus, and cumulus clouds also exert significant cooling influences on the planet but these effects seldom exceed 10 W m^{-2} in any given location (Fig. 7).

Multilayered cloud systems are found to significantly cool the planet by an average of -6.1 W m^{-2} , contributing nearly 44% of the global total $C_{SW,TOA}$ and nearly 49% of the global total $C_{LW,TOA}$. However, these effects vary substantially with geographic location. Multilayered cloud systems exert a strong cooling effect over the Pacific ITCZ, a warming effect over equatorial Africa, and a negligible effect over eastern India and Indonesia. This is a consequence of the fact that multilayered cloud pixels, as defined here, can consist of various combinations of high and low cloud whose frequency depends strongly on local environment. Nevertheless of the nine cloud types considered here, the spatial distribution of total $C_{Net,TOA}$ most closely resembles that from multilayered cloud systems that are likely the most challenging to capture in both passive observations and global models.

The net effect of clouds on TOA radiation is determined by the relative magnitude of the LW and SW effects. The radiative impacts of the single-layer cloud types are governed by a combination of their frequency and geometric and optical properties. Optically thin high clouds exert a net warming effect while optically thick, shallow clouds contribute a net cooling effect. The

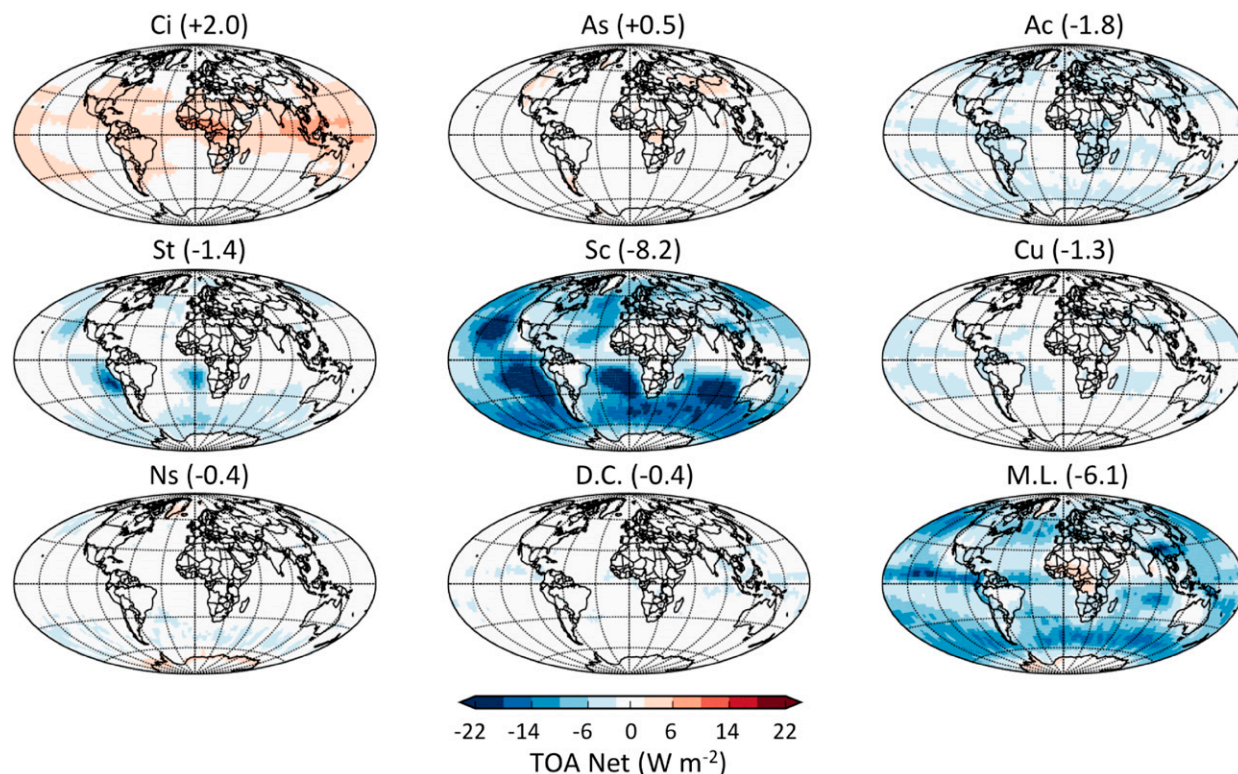


FIG. 7. Annual mean net cloud radiative effects at the TOA (W m^{-2}). Radiative effects are separated by cloud type determined based on 2BCLD classification. All flux data presented are from 2BFLX, 2007–10. The area-weighted global average (in W m^{-2}) is shown in parentheses.

transition between these regimes depends on both cloud height and optical depth but is decidedly skewed toward an albedo effect for most cloud types owing to the asymptotic behavior C_{LW} which saturates at relatively low optical depth. Only high, thin cirrus clouds and, to a much lesser extent, altostratus, exert positive net radiative effects globally.

The SW and LW radiative effects of each of cloud type are presented in Figs. 8 and 9, respectively. Single-layer cirrus are found to reduce SW absorption by only 0.8 W m^{-2} but decrease outgoing LW by 2.8 W m^{-2} resulting in a net warming effect of 2 W m^{-2} . In contrast, stratocumulus clouds reduce SW absorption by 10.4 W m^{-2} on the global annual mean, an effect nearly five times stronger than their greenhouse effect noted above. While single-layer nimbostratus, altostratus, and deep convective clouds exert significant effects in both SW and LW radiation individually, these effects largely cancel over the midlatitudes and tropics resulting in comparatively weak global mean net radiative effects. Cloud shortwave effects at the TOA are dominated by the grid box mean cloud optical depth, which peaks in areas of frequent stratocumulus a few hundred kilometers off the west coasts of North America, South

America, Africa, and Australia. Stratus exert significant C_{SW} but in smaller regions confined closer to the coasts while altostratus and nimbostratus exert strong C_{SW} in the higher-latitude storm tracks. Once again, infrequent single-layer deep convective clouds lead to a relatively small net SW radiative effect that is confined to the ITCZ and west Pacific.

Cloud longwave effects are generally dominated by the distribution of cloud-top height within each grid box peaking in regions where cirrus and altostratus are prevalent such as the intertropical and South Pacific convergence zones. At higher latitudes, frequent, relatively deep nimbostratus exert a significant longwave radiative effect that sums to a global impact comparable in magnitude to that of cirrus and altostratus. Perhaps less intuitively, clouds identified as stratocumulus in 2BCLD are also found to exert a substantial longwave radiative effect, owing to their large populations in storm tracks in North Atlantic and Pacific and over the southern oceans. While it may be debated whether it might be more appropriate to classify these clouds as cumulus, these results clearly indicate that, in sufficient numbers, purely liquid bearing clouds with high emissivities and tops warmer than 273 K exert a significant

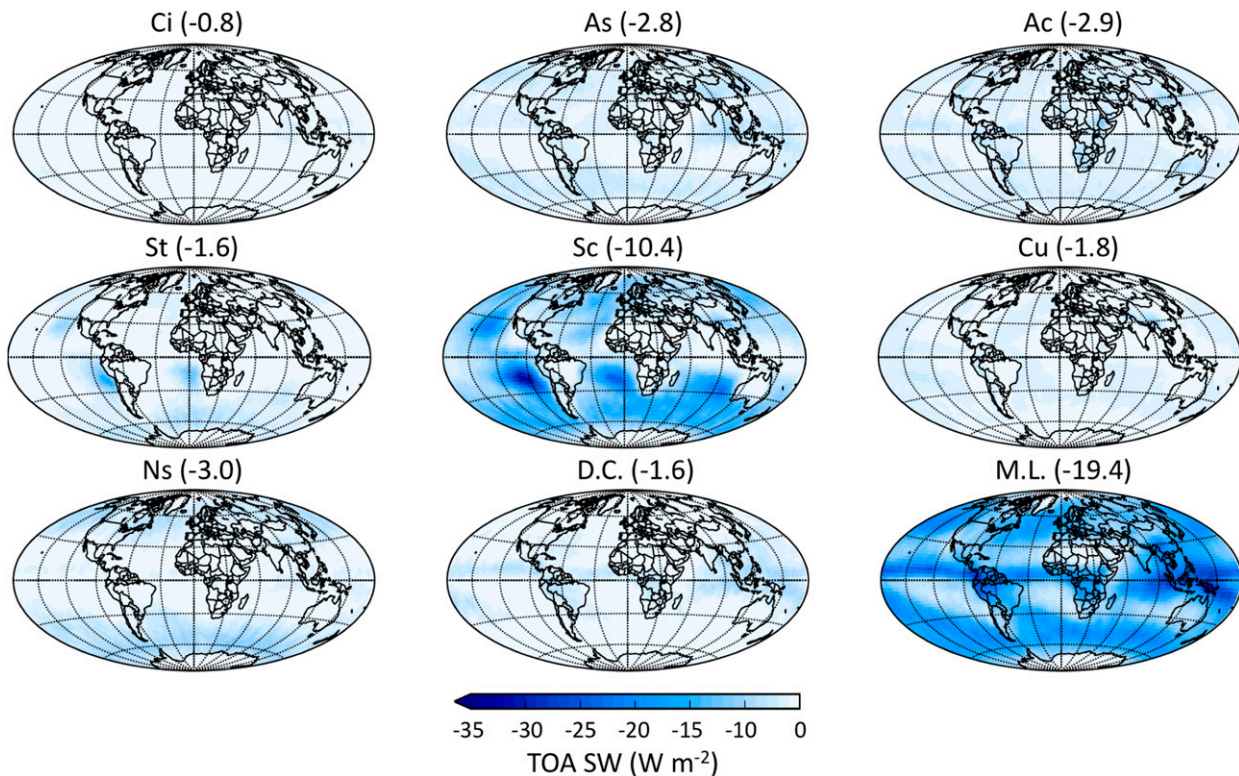


FIG. 8. As in Fig. 7, but for shortwave cloud radiative effects at the TOA (W m^{-2}).

global LW radiative effect at the TOA. At the fine resolution of individual *CloudSat* fields of view, single-layer deep convective clouds are observed relatively infrequently, leading to a muted impact on TOA radiation that is largely confined to the ITCZ and west Pacific.

While these findings generally follow basic physical principles governing cloud radiative effects that have been understood for several decades (Manabe and Strickler 1964; Stephens and Webster 1981; Ramanathan et al. 1989; Harrison et al. 1990; Stephens and Greenwald 1991; Gleckler et al. 1995), the active sensors aboard *CloudSat* and *CALIPSO* allow these effects to be quantified for individual cloud types defined based on explicit measures of their vertical structure. More importantly, *CloudSat* and *CALIPSO* provide unprecedented ability to identify pixels containing overlapping cloud layers, revealing that multilayered cloud systems dominate both $C_{\text{SW,TOA}}$ and $C_{\text{LW,TOA}}$, exerting albedo and greenhouse effects of -19.4 and 13.2 W m^{-2} , respectively. These radiative effects of multilayered cloud systems bear a strong resemblance to those of deep convective clouds in the tropics and stratocumulus clouds over midlatitude oceans, partially explaining the reduced influence deep convection globally relative to other studies (Oreopoulos and

Rossow 2011). At the pixel level, these observations reveal that systems that are traditionally generalized as “deep convection” really consist of a relatively small fraction of contiguous deep cores and a much larger fraction of multilayer clouds that often consist of cirrus overlying liquid clouds (Stephens and Wood 2007). While this distinction may seem inconsequential for TOA radiation balance, it has important implications for the structure of radiative heating in the atmosphere that can significantly influence atmospheric general circulation. Thus accurate estimates of the relative frequency of single- and multilayered clouds within convective systems have the potential to improve the accuracy of climate models (Chepfer et al. 2008; Naud et al. 2010).

2) SEASONAL VARIATION OF CLOUD RADIATIVE EFFECTS

Cloud cover, environmental characteristics, and solar insolation all vary substantially over the course of the year imparting a strong seasonality on net cloud radiative effects. For historical context, wherever possible the seasonal variability in cloud radiative effects are loosely grouped into cloud types that parallel those adopted more than 25 years ago by Ockert-Bell and Hartmann

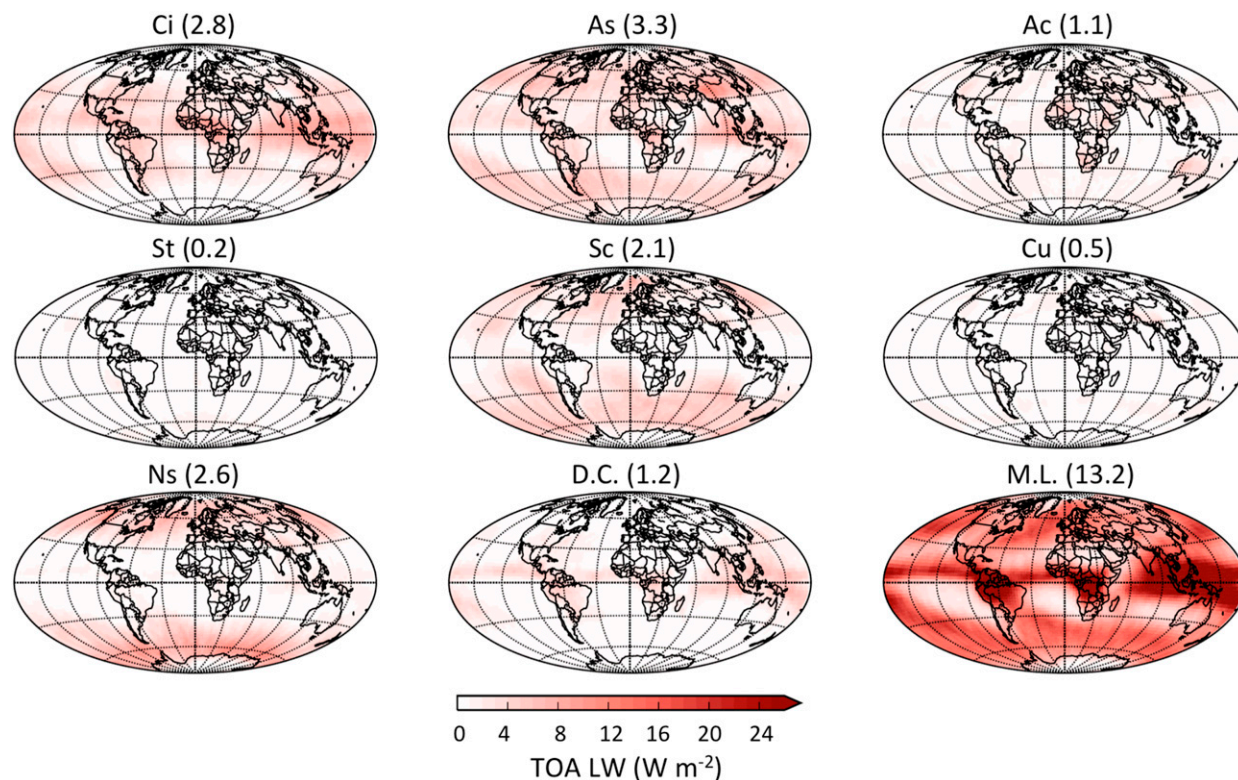


FIG. 9. As in Fig. 7, but for longwave cloud radiative effects at the TOA (W m^{-2}).

(1992) and Hartmann et al. (1992) to illustrate the evolution of the perspective provided by earlier passive instruments into that from modern radar and lidar observations. The most logical grouping is illustrated in Fig. 1 that highlights the new information provided by spaceborne active sensors. The five cloud types on the left correspond to the cloud-top pressure and visible optical depth–based cloud type definitions used by Hartmann et al. (1992). Those on the right illustrate where each of the nine 2BCLD *CloudSat* and *CALIPSO* vertical structure–based classes resides on this diagram. Given that there is no 1:1 relationship between physical height and pressure and the optical depths of the 2BCLD cloud types are variable, the axes on the right-hand chart have been replaced with qualitative indicators of increasing cloud height and optical thickness. Nevertheless, Fig. 10 illustrates how active sensors allow further distinctions to be made based on quantitative cloud top and base information and explicit detection of multiple cloud layers. Lacking such information, ISCCP cloud types were primarily based on estimates of cloud top height and total optical thickness and made no distinction between single and multilayered cloud systems, often misinterpreting the latter as midlevel clouds (Mace et al. 2009). More modern clustering techniques

make use of spatial structure information to better distinguish cumuliform and stratiform cloud types but have not fully resolved issues associated with misinterpreting multilayered cloud systems (Tselioudis and Jakob 2002; Oreopoulos and Rossow 2011). By contrast, vertically resolved measurements from *CloudSat* and *CALIPSO* are able to distinguish multilayered cloud systems from deep convective and midthick clouds as well as to subdivide mid- and low-level cloud types into altocumulus, altostratus, cumulus, stratocumulus, and stratus based on their vertical and horizontal extents, as shown in Fig. 1b.

Figure 10 compares zonal mean distributions of TOA SW, LW, and net CRE in Northern Hemisphere winter and summer defined as December–February (DJF) and June–August (JJA), respectively. Total zonal mean SW CRE (Figs. 10a,b) is approximately mirrored about the equator in DJF compared to JJA, owing to the shift in solar illumination between the hemispheres as expected. However, significant asymmetries exist at higher latitudes where shortwave effects are considerably more pronounced in the Southern Hemisphere in DJF due to enhanced solar reflection from ubiquitous marine clouds in the Southern Ocean. This asymmetry can be largely attributed to increased effects of stratocumulus clouds

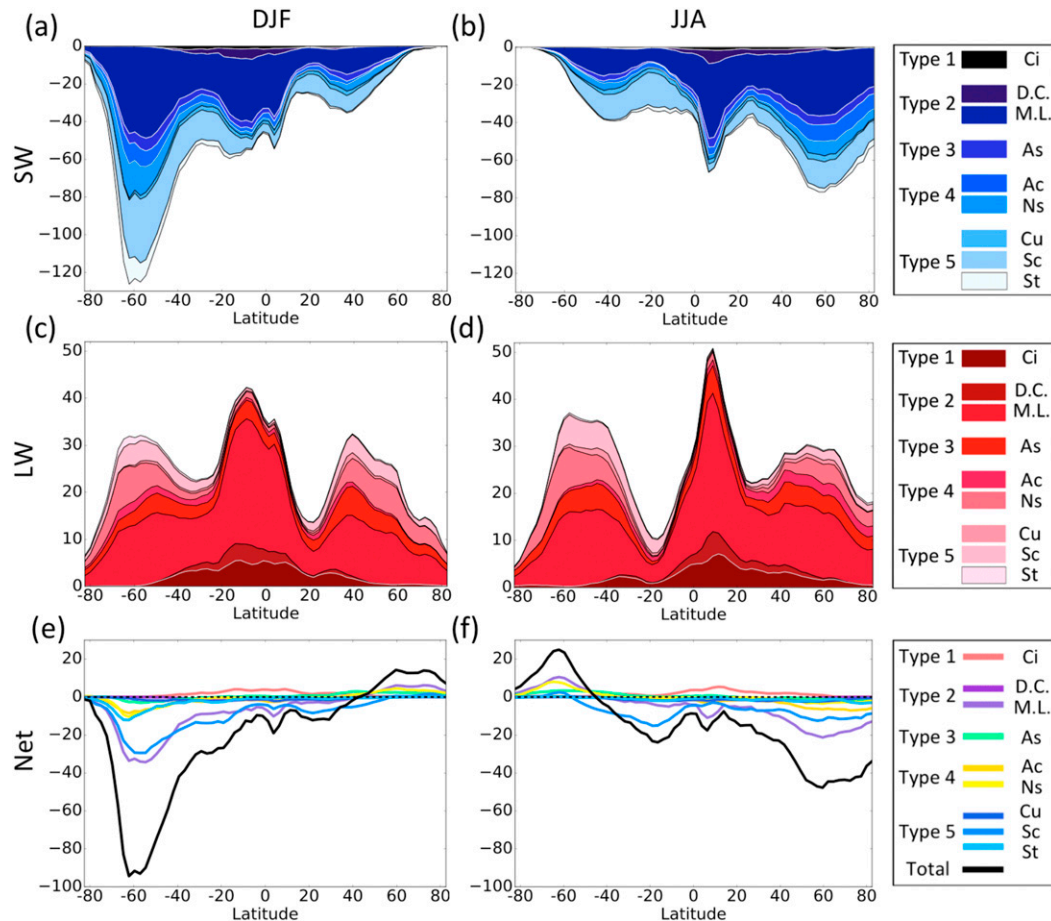


FIG. 10. Seasonal zonal mean cloud radiative effects at the TOA (W m^{-2}). Radiative effects are separated by cloud type determined based on 2BCLD classification. Seasons are defined as December–February (DJF) and June–August (JJA). All flux data are from 2BFLX, 2007–10.

that exert nearly 3 times as much SW CRE over the Southern Oceans than at similar latitudes in the Northern Hemisphere owing to the substantial difference in land fraction between the hemispheres.

By contrast, Figs. 10c and 10d show that the LW CRE is far more symmetric between the hemispheres with a maximum tracking the migration of the ITCZ and a distinct minimum in the subsidence regions at approximately 20° latitude in the winter hemisphere. This results in a hemispheric imbalance in net CRE. Not surprisingly, deep convective clouds and isolated cirrus dominate single-layered clouds effects on $C_{\text{LW,TOA}}$ in the tropics while midlevel cloud types contribute significantly at midlatitudes. The LW CRE of single-layer high clouds are, however, confined to tropical regions and considerably reduced relative to estimates from passive sensors owing to the explicit distinction between single- and multilayered systems enabled by active sensors. This is in contrast to the perspective from

passive sensors suggesting nearly equal contributions are made by high-thin clouds and high-thick clouds (e.g., Hartmann et al. 1992; Oreopoulos and Rossow 2011).

Figures 10e and 10f demonstrate that SW radiative effects dominate net cloud radiative effects at the TOA at most latitudes in both hemispheres with the exception of the polar regions in the winter hemisphere where nimbostratus and multilayered cloud systems induce a net heating over the ice caps. While it is well understood that clouds exert a positive net CRE in polar night, the magnitude of this effect has been very difficult to quantify with passive sensors, let alone isolating the effects of different cloud types. Here we find that cloud heating reaches a peak of more than 20 W m^{-2} over the Southern Hemisphere sea ice at 65°S before decreasing substantially over the interior of the Antarctic ice sheet. Conversely, clouds are found to warm the Arctic in winter by a more uniform 15 W m^{-2} poleward of 60°N .

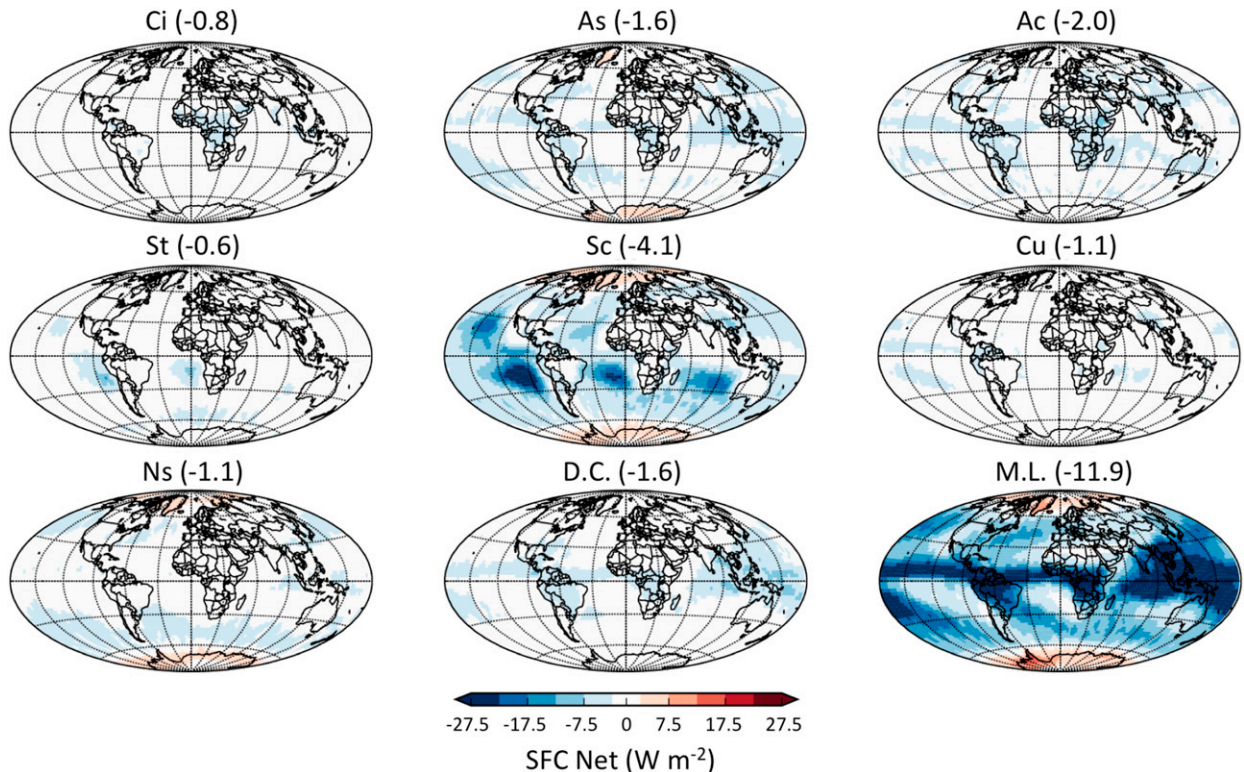


FIG. 11. As in Fig. 7, but for net cloud radiative effects at the surface (W m^{-2}).

Globally, stratocumulus and multilayered clouds contribute nearly equally to net CRE at the TOA, each imparting a large net cooling to Earth's energy budget. This can be contrasted with previous work that suggested that low clouds dominate the net radiative effect, with midlevel clouds providing the second-largest contribution. This emphasizes the value of spaceborne active sensors for resolving the ambiguity introduced in assigning multilayered systems by cloud-top pressure and optical depth (Mace et al. 2006, 2009). Scenes that contain a combination of high and low cloud are frequently misclassified as optically thick midlevel cloud by passive sensors (Marchand et al. 2010; Mace and Wrenn 2013). This has important implications for evaluating cloud distributions and their resultant radiative effects in global models. Vertically resolved measurements from *CloudSat* and *CALIPSO* offer new capability to resolve such ambiguities enabling new methods of cloud partitioning that may provide a robust understanding of the radiative effects of complex multilayered cloud types.

b. Surface

Clouds also strongly impact the surface energy balance by modulating radiative heat exchanges between

the atmosphere, land surface, and the ocean (Zhang et al. 1995; Bony et al. 1997; Wild et al. 2013). In fact, more than 90% of the excess energy in the climate system due to increased greenhouse gas concentrations is absorbed at the surface where clouds play a critical role in modulating radiative fluxes (Trenberth et al. 2009, 2014). However, current estimates of surface energy budget are poorly resolved because passive sensors lack the ability to penetrate optically thick clouds and quantify cloud base height. Models also exhibit large biases in radiative fluxes at the surface relative to ground-based measurements, some of which may be associated with cloud base heights (Garratt 2001; Wild et al. 2001; Wild 2005, 2008; Li et al. 2013; Wild et al. 2013). The accurate cloud base information provided by *CloudSat* and *CALIPSO* allows more robust estimates of how clouds influence the surface energy balance (L'Ecuyer et al. 2009; Stephens et al. 2012).

Figures 11–13 show the global distributions of $C_{\text{Net,SFC}}$, $C_{\text{SW,SFC}}$, and $C_{\text{LW,SFC}}$ derived from 2BFLX from each cloud type over 2007–10. Most clouds exert larger net cooling effects at the surface (Fig. 11) compared to the TOA (Fig. 7). The exception is stratus and stratocumulus clouds that enhance LW emission to the surface offsetting a significant fraction of their SW

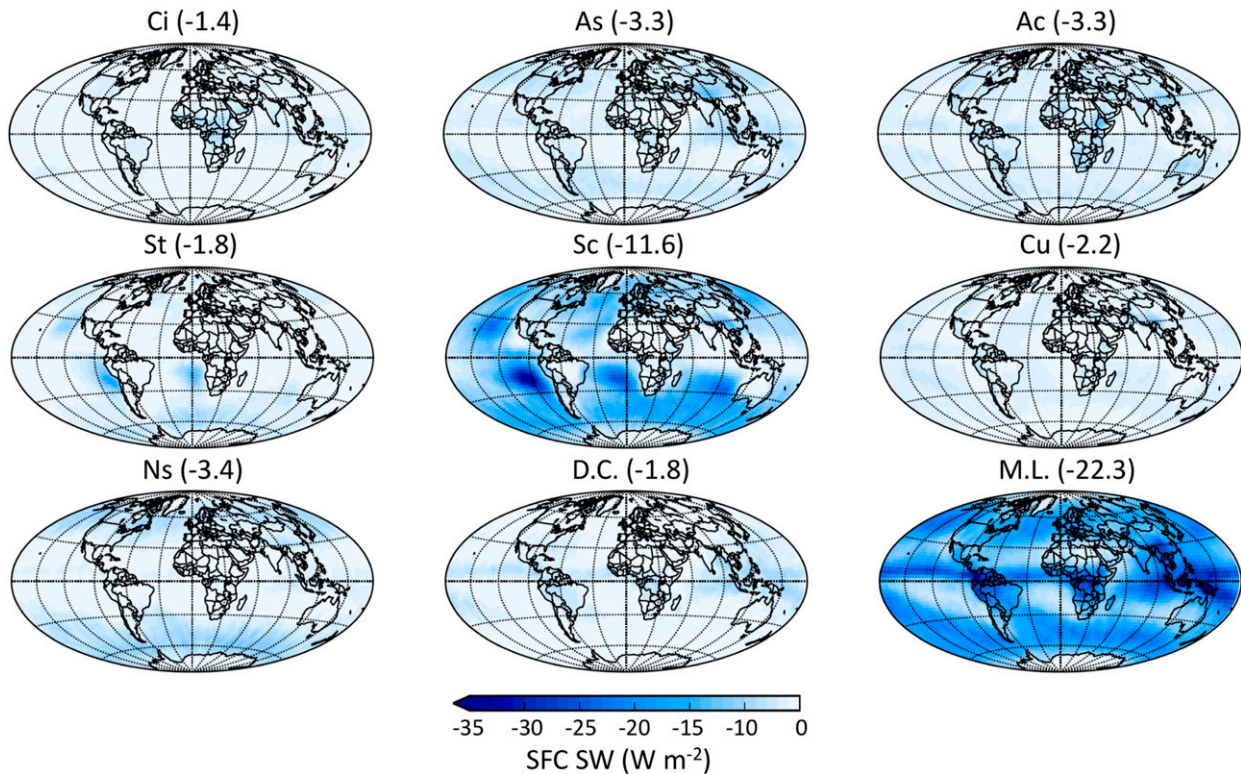


FIG. 12. As in Fig. 7, but for shortwave cloud radiative effects at the surface (W m^{-2}).

cooling effect. On the global annual mean, multilayered cloud systems represent the single largest source of cooling in Earth's surface energy budget with an estimated surface net CRE of -11.9 W m^{-2} . Stratocumulus clouds exert the second strongest net cooling at the surface (-4.1 W m^{-2}), only half as strong as their net effect at the TOA. All cloud types, especially, stratiform clouds and multilayered cloud systems, are found to exert a net warming effect over polar regions where enhanced longwave emission exceeds impacts on SW absorption owing to the reflective snow and ice surfaces and reduced annual mean solar insolation (Pavolonis and Key 2003).

It is clear from Figs. 12 and 13 that longwave heating dominates the difference in CRE between the TOA and surface. Figure 12 shows that the spatial patterns of $C_{\text{SW,SFC}}$ and $C_{\text{SW,TOA}}$ are very similar even though each cloud type exerts larger shortwave cooling effect at the surface than the TOA owing to additional absorption of SW radiation. The greatest contributions to $C_{\text{SW,SFC}}$ are, therefore, once again from multilayered cloud systems (-22.3 W m^{-2}) and stratocumulus clouds (-11.6 W m^{-2}) as at the TOA. On the other hand, $C_{\text{LW,SFC}}$ (Fig. 13) exhibits distinctly different patterns from the TOA (Fig. 9). For example, cirrus clouds, deep

convective clouds, and multilayered cloud systems exert much greater longwave radiative effects at the TOA than at the surface. Stratocumulus, stratus, and cumulus clouds, on the other hand, exert significant LW warming at the surface especially over subtropical and mid-latitude oceans where they enhance longwave emission to the surface at warm temperatures that correspond to their low cloud bases and large optical thicknesses (Mülmenstädt et al. 2018).

Global estimates of the zonal mean CRE at the surface are displayed in Fig. 14. Overall, there is closer symmetry between the CRE in DJF and in JJA at the surface than at the TOA. The zonal distribution of $C_{\text{SW,SFC}}$ (Figs. 14a,b) is similar to $C_{\text{SW,TOA}}$ (Figs. 10a,b), but with a larger magnitude. $C_{\text{SW,SFC}}$ peaks in DJF over the Southern Ocean where it approaches -140 W m^{-2} on the seasonal mean. The zonal distribution of $C_{\text{LW,SFC}}$ is substantially different from $C_{\text{LW,TOA}}$ exhibiting a pronounced minimum in the tropics owing to both a relatively low fraction of optically thick low clouds and the effects of water vapor that mask cloud emission to the surface. LW CRE increases at the surface over midlatitudes especially over the southern oceans where clouds enhance LW emission to the surface by nearly 60 W m^{-2} in both summer and winter causing a substantial

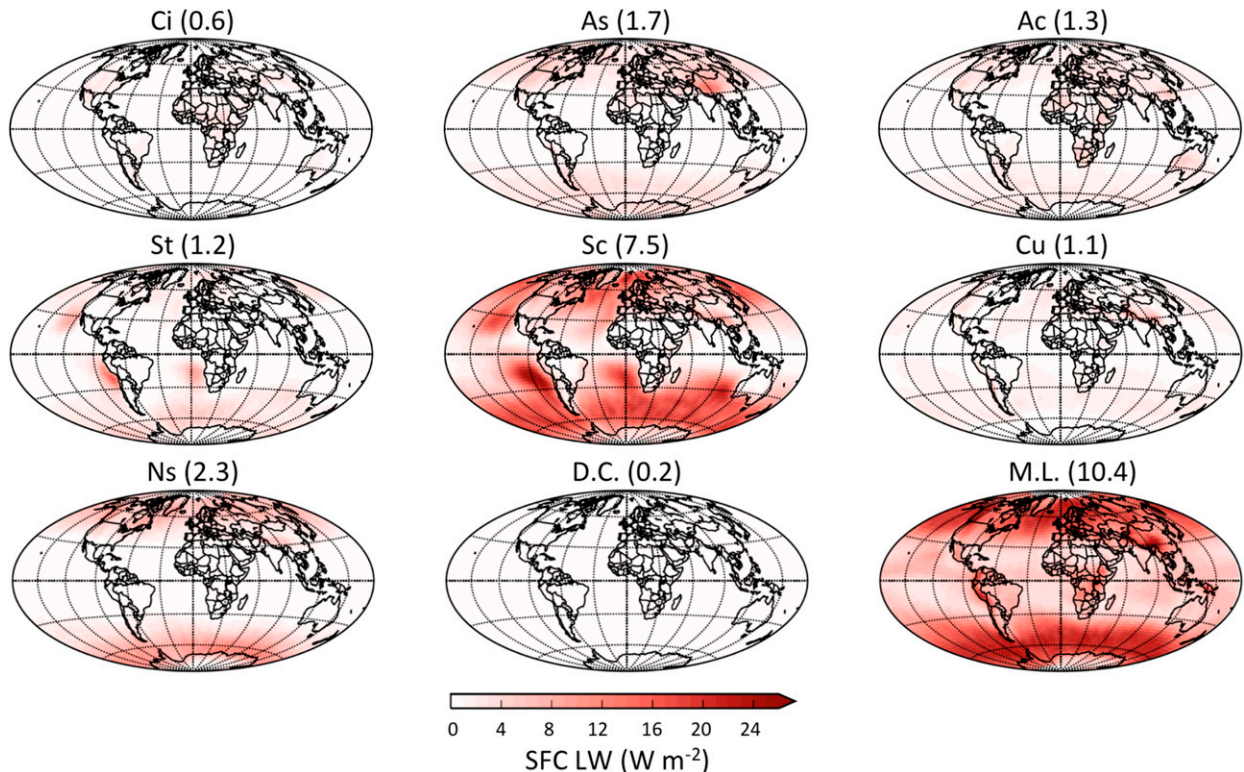


FIG. 13. As in Fig. 7, but for longwave cloud radiative effects at the surface (W m^{-2}).

seasonal oscillation in net cloud radiative effects at the surface (Figs. 14c,d).

Figures 14e and 14f indicate that clouds strongly cool the surface in the summer hemisphere while exerting somewhat smaller warming effects in the winter hemisphere. Thus the seasonal contrast in solar insolation between the hemispheres is muted at the surface (Rossow and Zhang 1995). The largest annual cycle of net CRE at the surface occurs over the southern oceans where clouds exert substantial warming in JJA and exert the strongest seasonal-mean net cooling observed anywhere on Earth in DJF. This results in a 125 W m^{-2} variation in net radiation absorbed at the surface over the annual cycle. When integrated over each hemisphere, this alternating cloud heating and cooling between winter and summer leads to about 100 W m^{-2} of relative cooling in the summer hemisphere offsetting a substantial fraction of the seasonal hemispheric imbalance in solar insolation.

4. Discussion and conclusions

This work updates global observational estimates of cloud impacts on the global radiation balance in light of the new vertically resolved cloud information from *CloudSat* and *CALIPSO*. While this topic is far from

new, these active sensors provide more robust information for separating single-layered and multilayered cloud systems according to their spatial and vertical structure than previous available. We calculate the radiative effects of nine distinct cloud types using the fifth release 2B-FLXHR-lidar product, which yields high horizontal and vertical resolution ($1.4 \times 1.7 \text{ km}^2$ and 240 m, respectively) radiative flux and heating rate profiles consistent with *CloudSat*, *CALIPSO*, MODIS, and AMSR-E observations. On the annual mean, clouds are found to exert a net cooling of $-17.1 \pm 4.2 \text{ W m}^{-2}$. This results from $-44.2 \pm 2 \text{ W m}^{-2}$ of SW reflection and $27.1 \pm 3.7 \text{ W m}^{-2}$ of enhanced LW heating, globally. Contrary to classical analyses, the greatest contributions to global CRE are found to come from multilayered clouds that are often misclassified as thick midlevel clouds in approaches that use passive sensors alone. Since multilayered cloud systems are often represented through crude overlap parameterizations in atmospheric general circulation models, these results reinforce the significant challenges involved in accurately modeling the impact of clouds on atmospheric circulations (Pincus et al. 2006; Naud et al. 2008; Mace et al. 2009; Shonk et al. 2012). The decomposition of cloud radiative effects into the vertically resolved cloud types and multilayered cloud systems presented here may

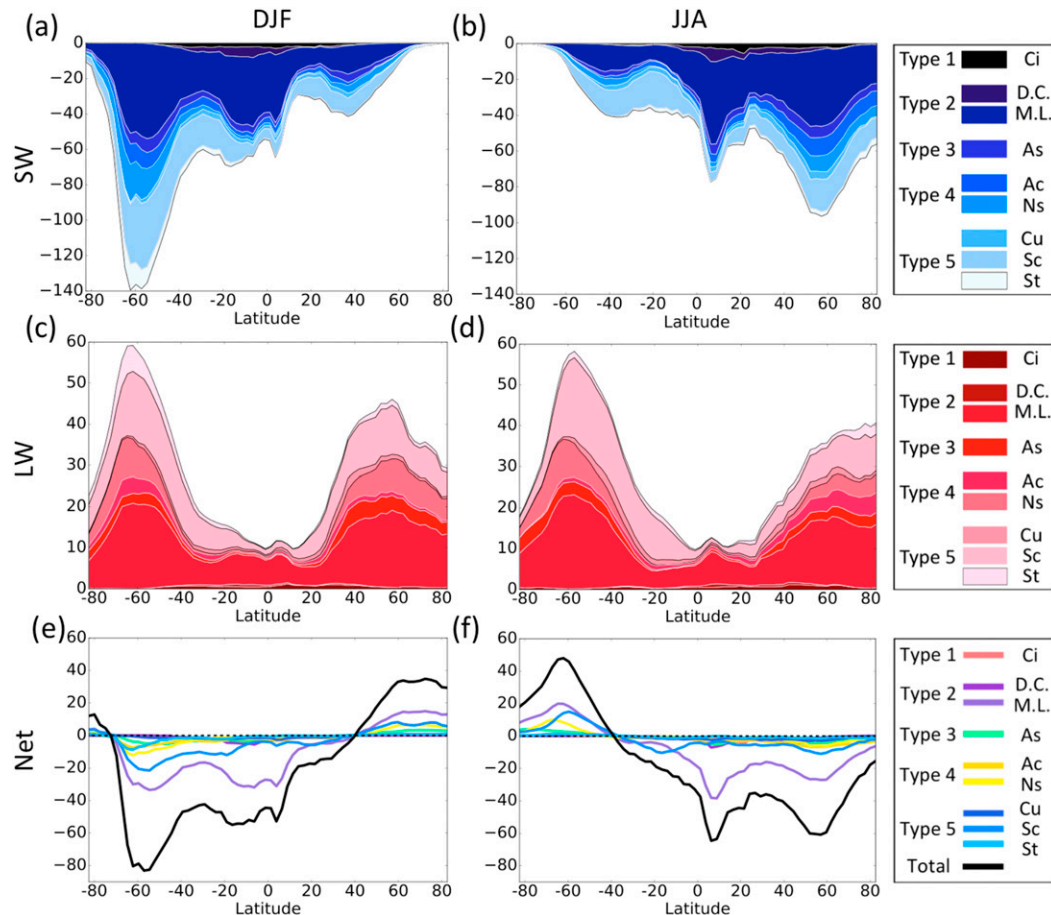


FIG. 14. As in Fig. 10, but for seasonal zonal mean cloud radiative effects at the surface (W m^{-2}).

offer a potential pathway for evaluating the distribution of cloud radiative effects and column heating rates within AGCMs in light of the new vertical structure information provided by spaceborne active sensors in much the same way as ISCCP and ERBE did three decades ago (Cess et al. 1989, 1990; Harrison et al. 1990; Webb et al. 2001; Zhang et al. 2005; Wyant et al. 2006).

This work also leverages *CloudSat* and *CALIPSO* cloud boundary information to discern the influence of cloud-type variations on radiation balance at Earth's surface, a critical factor in modulating the disposition of excess energy in the climate system. The global annual net cloud radiative effect at the surface is estimated to be $-24.8 \pm 8.7 \text{ W m}^{-2}$. SFC SW CRE exhibits a very similar spatial pattern as TOA SW CRE but is enhanced by 7 to $-51.1 \pm 7.8 \text{ W m}^{-2}$ owing to increased atmospheric absorption by clouds. On the other hand, the global mean LW CRE at the surface ($26.3 \pm 3.8 \text{ W m}^{-2}$) is almost identical to that at the TOA but exhibits a markedly different spatial pattern, reflecting the fact that SFC LW CRE derives from enhanced emission from

liquid water near the surface. This implies that, while cloud SW effects govern cloud impacts on total atmospheric heating, LW effects govern its redistribution. This result is explored in much greater detail in a companion paper (i.e., Part II of this paper, Hang et al. 2019).

It is further shown that multilayered clouds also dominate CRE at the surface, enhancing surface longwave radiation by 10.4 W m^{-2} and reducing surface shortwave radiation by 22.3 W m^{-2} . Stratocumulus clouds also strongly reduce surface shortwave radiation by 11.6 W m^{-2} but nearly 60% of this is offset by enhanced LW emission. These results provide valuable constraints on TOA and surface energy balance and hint at the different roles distinct cloud types may play in atmospheric heating. They clearly confirm that clouds with similar TOA radiative signatures can have very different impacts at the surface. This is consistent with the fact that distinct cloud types exhibit distinct vertical heating profiles in the atmosphere and, by extension, exert distinct influences on large-scale circulations (Mace and Wrenn 2013). Although it is beyond the

		Global	Ci	As	Ac	St	Sc	Cu	Ns	D.C.	M.L.	Total
TOA	CF		7.9	4.5	3.3	2.3	15.5	3.0	3.7	0.8	29.9	70.8
	CRE _{SW}		-0.8	-2.8	-2.9	-1.6	-10.4	-1.8	-3.0	-1.6	-19.4	-44.2
	CRE _{LW}		2.8	3.3	1.1	0.2	2.1	0.5	2.6	1.2	13.2	27.1
	CRE _{Net}		2.0	0.5	-1.8	-1.4	-8.3	-1.3	-0.4	-0.4	-6.2	-17.1
	NH											
	CF		9.1	5.1	3.5	1.5	12.3	3.0	3.4	0.9	30.5	69.3
	CRE _{SW}		-0.9	-3.0	-3.0	-0.9	-7.5	-1.9	-2.5	-1.8	-19.1	-40.4
	CRE _{LW}		3.2	3.6	1.3	0.2	1.6	0.5	2.3	1.3	13.6	27.6
	CRE _{Net}		2.3	0.6	-1.8	-0.7	-5.9	-1.3	-0.2	-0.4	-5.4	-12.8
	SH											
	CF		6.7	3.9	3.2	3.1	18.6	3.1	4.0	0.6	29.3	72.4
	CRE _{SW}		-0.8	-2.8	-2.6	-2.4	-13.5	-1.9	-3.4	-1.3	-19.5	-48.1
	CRE _{LW}		2.3	3.0	1.0	0.4	2.7	0.6	2.8	1.0	12.9	26.7
	CRE _{Net}		1.6	0.4	-1.7	-2.0	-10.9	-1.3	-0.5	-0.3	-6.7	-21.4
SFC	Global		Ci	As	Ac	St	Sc	Cu	Ns	D.C.	M.L.	All
	CF		7.9	4.5	3.3	2.3	15.5	3.0	3.7	0.8	29.9	70.8
	CRE _{SW}		-1.4	-3.3	-3.3	-1.8	-11.6	-2.2	-3.4	-1.8	-22.3	-51.1
	CRE _{LW}		0.6	1.7	1.3	1.2	7.5	1.1	2.3	0.2	10.4	26.3
	CRE _{Net}		-0.8	-1.6	-2.0	-0.6	-4.1	-1.1	-1.1	-1.6	-11.9	-24.8
	NH											
	CF		9.1	5.1	3.5	1.5	12.3	3.0	3.4	0.9	30.5	69.3
	CRE _{SW}		-2.0	-3.7	-3.5	-1.0	-8.7	-2.3	-3.0	-1.9	-22.8	-49.0
	CRE _{LW}		0.8	1.9	1.4	0.8	5.5	1.1	2.2	0.3	10.1	24.1
	CRE _{Net}		-1.2	-1.8	-2.1	-0.2	-3.3	-1.2	-0.8	-1.6	-12.7	-24.9
	SH											
	CF		6.7	3.9	3.2	3.1	18.6	3.1	4.0	0.6	29.3	72.4
	CRE _{SW}		-1.2	-3.0	-3.1	-2.6	-14.9	-2.2	-3.8	-1.4	-22.0	-54.1
	CRE _{LW}		0.5	1.4	1.1	1.6	9.4	1.1	2.5	0.2	10.6	28.4
	CRE _{Net}		-0.7	-1.6	-1.9	-1.0	-5.5	-1.1	-1.3	-1.2	-11.4	-25.7

FIG. 15. Summary of type-separated global, Northern Hemisphere, and Southern Hemisphere annual mean cloud fraction (%) and cloud radiative effect (W m^{-2}) at the TOA and surface. All data presented are from 2BFLX, 2007–10.

scope of the current study, *CloudSat* and *CALIPSO* provide the vertical resolution required to examine the influence of cloud morphology on the spatial and vertical distribution of heating within the atmosphere (Mather and McFarlane 2009; Protat et al. 2014; Ham et al. 2017).

Consistent with other recent work, a hemispheric asymmetry in CRE is observed. This is illustrated in Fig. 15, which summarizes all of the numerical findings from this paper and reports the radiative impacts of each vertical structure-based cloud type at the TOA and SFC for each hemisphere separately. At the TOA, clouds cool the Northern Hemisphere by -12.8 W m^{-2} while cooling the Southern Hemisphere by -21.4 W m^{-2} . This asymmetry is primarily caused by the strong radiative cooling from stratocumulus over the Southern Ocean

during local summer (Fasullo and Trenberth 2008; Stephens et al. 2016). Stratocumulus clouds exert almost twice as much SW cooling at the TOA (-13.5 W m^{-2}) in the Southern Hemisphere as they do in the Northern Hemisphere (-7.5 W m^{-2}).

Possibly more striking, however, is the fact that there is no accompanying hemispheric imbalance in cloud radiative effects at the surface. On the annual mean, the stronger summertime surface SW cooling from stratocumulus is canceled by enhanced LW heating from low clouds year-round. This suggests that the asymmetry in cloud radiative effects is primarily realized in the atmosphere, influencing atmospheric heat transport across the equator much more so than in the oceans. As noted by many others, understanding and modeling this hemispheric asymmetry is critical for accurately

representing atmospheric circulations in global models (Frierson et al. 2013; Loeb et al. 2016; Stephens et al. 2016). The results presented here reinforce the need to resolve model low cloud biases in the southern oceans and add an imperative to assess and improve the representation of multilayered cloud systems using active sensors.

Acknowledgments. This work was supported by NASA Grants NNX13AQ32G and NNX16AO93G. We also recognize the important contributions of Phil Partain and the CloudSat Data Processing Center (DPC). All CloudSat data were acquired through the DPC and can be accessed at <http://www.cloudsat.cira.colostate.edu>.

REFERENCES

- Ackerman, S., R. Holz, R. Frey, E. Eloranta, B. Maddux, and M. McGill, 2008: Cloud detection with MODIS. Part II: Validation. *J. Atmos. Oceanic Technol.*, **25**, 1073–1086, <https://doi.org/10.1175/2007JTECHA1053.1>.
- Ackerman, T. P., and G. M. Stokes, 2003: The Atmospheric Radiation Measurement program. *Phys. Today*, **56**, 38, <https://doi.org/10.1063/1.1554135>.
- Allan, R. P., 2011: Combining satellite data and models to estimate cloud radiative effect at the surface and in the atmosphere. *Meteor. Appl.*, **18**, 324–333, <https://doi.org/10.1002/met.285>.
- Bacmeister, J., and G. Stephens, 2011: Spatial statistics of likely convective clouds in Cloudsat data. *J. Geophys. Res.*, **116**, D04104, <https://doi.org/10.1029/2010JD014444>.
- Bodas-Salcedo, A., and Coauthors, 2014: Origins of the solar radiation biases over the Southern Ocean in CFMIP2 models. *J. Climate*, **27**, 41–56, <https://doi.org/10.1175/JCLI-D-13-00169.1>.
- Bony, S., K.-M. Lau, and Y. C. Sud, 1997: Sea surface temperature and large-scale circulation influences on tropical greenhouse effect and cloud radiative forcing. *J. Climate*, **10**, 2055–2077, [https://doi.org/10.1175/1520-0442\(1997\)010<2055:SSTALS>2.0.CO;2](https://doi.org/10.1175/1520-0442(1997)010<2055:SSTALS>2.0.CO;2).
- , and Coauthors, 2006: How well do we understand and evaluate climate change feedback processes? *J. Climate*, **19**, 3445–3482, <https://doi.org/10.1175/JCLI3819.1>.
- Calisto, M., D. Folini, M. Wild, and L. Bengtsson, 2014: Cloud radiative forcing intercomparison between fully coupled CMIP5 models and CERES satellite data. *Ann. Geophys.*, **32**, 793–807, <https://doi.org/10.5194/angeo-32-793-2014>.
- Cess, R. D., and Coauthors, 1989: Interpretation of cloud-climate feedback as produced by 14 atmospheric general circulation models. *Science*, **245**, 513–516, <https://doi.org/10.1126/science.245.4917.513>.
- , and Coauthors, 1990: Intercomparison and interpretation of climate feedback processes in 19 atmospheric general circulation models. *J. Geophys. Res.*, **95**, 16 601–16 615, <https://doi.org/10.1029/JD095iD10p16601>.
- Chan, M. A., and J. C. Comiso, 2011: Cloud features detected by MODIS but not by CloudSat and CALIOP. *Geophys. Res. Lett.*, **38**, L24813, <https://doi.org/10.1029/2011GL050063>.
- Chen, T., W. B. Rossow, and Y. Zhang, 2000: Radiative effects of cloud-type variations. *J. Climate*, **13**, 264–286, [https://doi.org/10.1175/1520-0442\(2000\)013<0264:REOCTV>2.0.CO;2](https://doi.org/10.1175/1520-0442(2000)013<0264:REOCTV>2.0.CO;2).
- Chepfer, H., S. Bony, D. Winker, M. Chiriaco, J.-L. Dufresne, and G. Sèze, 2008: Use of CALIPSO lidar observations to evaluate the cloudiness simulated by a climate model. *Geophys. Res. Lett.*, **35**, L15704, <https://doi.org/10.1029/2008GL034207>.
- Comstock, J. M., T. P. Ackerman, and G. G. Mace, 2002: Ground-based lidar and radar remote sensing of tropical cirrus clouds at Nauru Island: Cloud statistics and radiative impacts. *J. Geophys. Res.*, **107**, 4714, <https://doi.org/10.1029/2002JD002203>.
- Deng, M., G. G. Mace, Z. Wang, and R. P. Lawson, 2013: Evaluation of several A-Train ice cloud retrieval products with in situ measurements collected during the SPARTICUS campaign. *J. Appl. Meteor. Climatol.*, **52**, 1014–1030, <https://doi.org/10.1175/JAMC-D-12-054.1>.
- Fasullo, J. T., and K. E. Trenberth, 2008: The annual cycle of the energy budget. Part II: Meridional structures and poleward transports. *J. Climate*, **21**, 2313–2325, <https://doi.org/10.1175/2007JCLI1936.1>.
- Frierson, D. M., and Coauthors, 2013: Contribution of ocean overturning circulation to tropical rainfall peak in the Northern Hemisphere. *Nat. Geosci.*, **6**, 940–944, <https://doi.org/10.1038/ngeo1987>.
- Garratt, J., 2001: Clear-sky longwave irradiance at the Earth's surface—Evaluation of climate models. *J. Climate*, **14**, 1647–1670, [https://doi.org/10.1175/1520-0442\(2001\)014<1647:CSLIAT>2.0.CO;2](https://doi.org/10.1175/1520-0442(2001)014<1647:CSLIAT>2.0.CO;2).
- Gleckler, P., and Coauthors, 1995: Cloud-radiative effects on implied oceanic energy transports as simulated by atmospheric general circulation models. *Geophys. Res. Lett.*, **22**, 791–794, <https://doi.org/10.1029/95GL00113>.
- Gupta, S. K., N. A. Ritchey, A. C. Wilber, C. H. Whitlock, G. G. Gibson, and P. W. Stackhouse Jr., 1999: A climatology of surface radiation budget derived from satellite data. *J. Climate*, **12**, 2691–2710, [https://doi.org/10.1175/1520-0442\(1999\)012<2691:ACOSRB>2.0.CO;2](https://doi.org/10.1175/1520-0442(1999)012<2691:ACOSRB>2.0.CO;2).
- Hahn, C. J., and S. G. Warren, 1999: Extended edited synoptic cloud reports from ships and land stations over the globe, 1952–1996. Environmental Sciences Division, Office of Biological and Environmental Research, U.S. Department of Energy, <https://doi.org/10.3334/CDIAC/cli.ndp026c>.
- Ham, S.-H., and Coauthors, 2017: Cloud occurrences and cloud radiative effects (CREs) from CERES-CALIPSO-CloudSat-MODIS (CCCM) and CloudSat radar-lidar (RL) products. *J. Geophys. Res.*, **122**, 8852–8884, <https://doi.org/10.1002/2017JD026725>.
- Hang, Y., T. S. L'Ecuyer, D. S. Henderson, A. V. Matus, and Z. Wang, 2019: Reassessing the effect of cloud type on Earth's energy balance in the age of active spaceborne observations. Part II: Atmospheric heating. *J. Climate*, **32**, 6219–6236, <https://doi.org/10.1175/JCLI-D-18-0754.1>.
- Harrison, E. F., P. Minnis, B. R. Barkstrom, V. Ramanathan, R. D. Cess, and G. G. Gibson, 1990: Seasonal variation of cloud radiative forcing derived from the Earth Radiation Budget Experiment. *J. Geophys. Res.*, **95**, 18 687–18 703, <https://doi.org/10.1029/JD095iD11p18687>.
- Hartmann, D., V. Ramanathan, A. Berroir, and G. Hunt, 1986: Earth radiation budget data and climate research. *Rev. Geophys.*, **24**, 439–468, <https://doi.org/10.1029/RG024i002p00439>.
- , M. E. Ockert-Bell, and M. L. Michelsen, 1992: The effect of cloud type on Earth's energy balance: Global analysis. *J. Climate*, **5**, 1281–1304, [https://doi.org/10.1175/1520-0442\(1992\)005<1281:TEOCTO>2.0.CO;2](https://doi.org/10.1175/1520-0442(1992)005<1281:TEOCTO>2.0.CO;2).
- Henderson, D. S., T. L'Ecuyer, G. Stephens, P. Partain, and M. Sekiguchi, 2013: A multisensor perspective on the radiative impacts of clouds and aerosols. *J. Appl. Meteor. Climatol.*, **52**, 853–871, <https://doi.org/10.1175/JAMC-D-12-025.1>.

- Howard, L., 1803: I. On the modifications of clouds, and on the principles of their production, suspension, and destruction; being the substance of an essay read before the Askesian Society in the session 1802–03. *Philos. Mag.*, **17** (65), 5–11, <https://doi.org/10.1080/14786440308676365>.
- , 1843: *Seven Lectures on Meteorology. A Second Edition Carefully Revised by the Author*. Harvey and Darton, London, 218 pp.
- Jakob, C., and G. Tselioudis, 2003: Objective identification of cloud regimes in the tropical western Pacific. *Geophys. Res. Lett.*, **30**, 2082, <https://doi.org/10.1029/2003GL018367>.
- Kato, S., S. Sun-Mack, W. F. Miller, F. G. Rose, Y. Chen, P. Minnis, and B. A. Wielicki, 2010: Relationships among cloud occurrence frequency, overlap, and effective thickness derived from CALIPSO and CloudSat merged cloud vertical profiles. *J. Geophys. Res.*, **115**, D00H28, <https://doi.org/10.1029/2009JD012277>.
- Kiehl, J. T., 1994: Clouds and their effects on the climate system. *Phys. Today*, **47**, 36–42, <https://doi.org/10.1063/1.881424>.
- L'Ecuyer, T. S., and J. H. Jiang, 2010: Touring the atmosphere aboard the A-Train. *Phys. Today*, **63**, 36–41, <https://doi.org/10.1063/1.3463626>.
- , N. B. Wood, T. Haladay, G. L. Stephens, and P. W. Stackhouse, 2008: Impact of clouds on atmospheric heating based on the R04 CloudSat fluxes and heating rates data set. *J. Geophys. Res.*, **113**, D00A15, <https://doi.org/10.1029/2008JD009951>.
- , W. Berg, J. Haynes, M. Lebsock, and T. Takemura, 2009: Global observations of aerosol impacts on precipitation occurrence in warm maritime clouds. *J. Geophys. Res.*, **114**, D09211, <https://doi.org/10.1029/2008JD011273>.
- Li, J.-L., D. Waliser, G. Stephens, S. Lee, T. L'Ecuyer, S. Kato, N. Loeb, and H.-Y. Ma, 2013: Characterizing and understanding radiation budget biases in CMIP3/CMIP5 GCMs, contemporary GCM, and reanalysis. *J. Geophys. Res.*, **118**, 8166–8184, <https://doi.org/10.1002/JGRD.50378>.
- Loeb, N. G., B. A. Wielicki, D. R. Doelling, G. L. Smith, D. F. Keyes, S. Kato, N. Manalo-Smith, and T. Wong, 2009: Toward optimal closure of the earth's top-of-atmosphere radiation budget. *J. Climate*, **22**, 748–766, <https://doi.org/10.1175/2008JCLI2637.1>.
- , H. Wang, A. Cheng, S. Kato, J. T. Fasullo, K.-M. Xu, and R. P. Allan, 2016: Observational constraints on atmospheric and oceanic cross-equatorial heat transports: Revisiting the precipitation asymmetry problem in climate models. *Climate Dyn.*, **46**, 3239–3257, <https://doi.org/10.1007/s00382-015-2766-z>.
- , and Coauthors, 2018: Clouds and the Earth's Radiant Energy System (CERES) energy balanced and filled (EBAF) top-of-atmosphere (TOA) edition-4.0 data product. *J. Climate*, **31**, 895–918, <https://doi.org/10.1175/JCLI-D-17-0208.1>.
- Mace, G. G., and F. J. Wrenn, 2013: Evaluation of the hydrometeor layers in the east and west Pacific within ISCCP cloud-top pressure–optical depth bins using merged CloudSat and CALIPSO data. *J. Climate*, **26**, 9429–9444, <https://doi.org/10.1175/JCLI-D-12-00207.1>.
- , and Coauthors, 2006: Cloud radiative forcing at the Atmospheric Radiation Measurement Program Climate Research Facility: 1. Technique, validation, and comparison to satellite-derived diagnostic quantities. *J. Geophys. Res.*, **111**, D11S90, <https://doi.org/10.1029/2005JD005921>.
- , Q. Zhang, M. Vaughan, R. Marchand, G. Stephens, C. Trepte, and D. Winker, 2009: A description of hydrometeor layer occurrence statistics derived from the first year of merged CloudSat and CALIPSO data. *J. Geophys. Res.*, **114**, D00A26, <https://doi.org/10.1029/2007JD009755>.
- Manabe, S., and R. F. Strickler, 1964: Thermal equilibrium of the atmosphere with a convective adjustment. *J. Atmos. Sci.*, **21**, 361–385, [https://doi.org/10.1175/1520-0469\(1964\)021<0361:TEOTAW>2.0.CO;2](https://doi.org/10.1175/1520-0469(1964)021<0361:TEOTAW>2.0.CO;2).
- Marchand, R., T. Ackerman, M. Smyth, and W. B. Rossow, 2010: A review of cloud top height and optical depth histograms from MISR, ISCCP, and MODIS. *J. Geophys. Res.*, **115**, D16206, <https://doi.org/10.1029/2009JD013422>.
- Mather, J. H., and S. A. McFarlane, 2009: Cloud classes and radiative heating profiles at the Manus and Nauru Atmospheric Radiation Measurement (ARM) sites. *J. Geophys. Res.*, **114**, D19204, <https://doi.org/10.1029/2009JD011703>.
- Matus, A. V., and T. S. L'Ecuyer, 2017: The role of cloud phase in Earth's radiation budget. *J. Geophys. Res. Atmos.*, **122**, 2559–2578, <https://doi.org/10.1002/2016JD025951>.
- McGill, M. J., M. A. Vaughan, C. R. Trepte, W. D. Hart, D. L. Hlavka, D. M. Winker, and R. Kuehn, 2007: Airborne validation of spatial properties measured by the CALIPSO lidar. *J. Geophys. Res.*, **112**, D20201, <https://doi.org/10.1029/2007JD008768>.
- Mülmenstädt, J., and Coauthors, 2018: Using CALIOP to estimate cloud-field base height and its uncertainty: The Cloud Base Altitude Spatial Extrapolator (CBASE) algorithm and dataset. *Earth Syst. Sci. Data*, **10**, 2279–2293, <https://doi.org/10.5194/ESSD-10-2279-2018>.
- Naud, C. M., A. Del Genio, G. G. Mace, S. Benson, E. E. Clothiaux, and P. Kollias, 2008: Impact of dynamics and atmospheric state on cloud vertical overlap. *J. Climate*, **21**, 1758–1770, <https://doi.org/10.1175/2007JCLI1828.1>.
- , —, M. Bauer, and W. Kovari, 2010: Cloud vertical distribution across warm and cold fronts in CloudSat–CALIPSO data and a general circulation model. *J. Climate*, **23**, 3397–3415, <https://doi.org/10.1175/2010JCLI3282.1>.
- Ockert-Bell, M. E., and D. L. Hartmann, 1992: The effect of cloud type on Earth's energy balance: Results for selected regions. *J. Climate*, **5**, 1157–1171, [https://doi.org/10.1175/1520-0442\(1992\)005<1157:TEOCTO>2.0.CO;2](https://doi.org/10.1175/1520-0442(1992)005<1157:TEOCTO>2.0.CO;2).
- Oreopoulos, L., and W. Rossow, 2011: The cloud radiative effects of International Satellite Cloud Climatology Project weather states. *J. Geophys. Res.*, **116**, D12202, <https://doi.org/10.1029/2010JD015472>.
- , N. Cho, D. Lee, and S. Kato, 2016: Radiative effects of global MODIS cloud regimes. *J. Geophys. Res.*, **121**, 2299–2317, <https://doi.org/10.1002/2015JD024502>.
- , —, and —, 2017: New insights about cloud vertical structure from CloudSat and CALIPSO observations. *J. Geophys. Res. Atmos.*, **122**, 9280–9300, <https://doi.org/10.1002/2017JD026629>.
- Pavolonis, M. J., and J. R. Key, 2003: Antarctic cloud radiative forcing at the surface estimated from the AVHRR polar pathfinder and ISCCP D1 datasets, 1985–93. *J. Appl. Meteor.*, **42**, 827–840, [https://doi.org/10.1175/1520-0450\(2003\)042<0827:ACRFAT>2.0.CO;2](https://doi.org/10.1175/1520-0450(2003)042<0827:ACRFAT>2.0.CO;2).
- Pincus, R., R. Hemler, and S. A. Klein, 2006: Using stochastically generated subcolumns to represent cloud structure in a large-scale model. *Mon. Wea. Rev.*, **134**, 3644–3656, <https://doi.org/10.1175/MWR3257.1>.
- Platnick, S., M. D. King, S. A. Ackerman, W. P. Menzel, B. A. Baum, J. C. Riedi, and R. A. Frey, 2003: The MODIS cloud products: Algorithms and examples from Terra. *IEEE Trans. Geosci. Remote Sens.*, **41**, 459–473, <https://doi.org/10.1109/TGRS.2002.808301>.
- Protat, A., and Coauthors, 2014: Reconciling ground-based and space-based estimates of the frequency of occurrence and

- radiative effect of clouds around Darwin, Australia. *J. Appl. Meteor. Climatol.*, **53**, 456–478, <https://doi.org/10.1175/JAMC-D-13-072.1>.
- Ramanathan, V., R. D. Cess, E. F. Harrison, P. Minnis, and B. R. Barkstrom, 1989: Cloud-radiative forcing and climate: Results from the Earth Radiation Budget Experiment. *Science*, **243**, 57–63, <https://doi.org/10.1126/science.243.4887.57>.
- Raschke, E., S. Kinne, W. B. Rossow, P. W. Stackhouse Jr., and M. Wild, 2016: Comparison of radiative energy flows in observational datasets and climate modeling. *J. Appl. Meteor. Climatol.*, **55**, 93–117, <https://doi.org/10.1175/JAMC-D-14-0281.1>.
- Rossow, W. B., and A. A. Lacis, 1990: Global, seasonal cloud variations from satellite radiance measurements. Part II: Cloud properties and radiative effects. *J. Climate*, **3**, 1204–1253, [https://doi.org/10.1175/1520-0442\(1990\)003<1204:GSCVFS>2.0.CO;2](https://doi.org/10.1175/1520-0442(1990)003<1204:GSCVFS>2.0.CO;2).
- , and Y.-C. Zhang, 1995: Calculation of surface and top of atmosphere radiative fluxes from physical quantities based on ISCCP data sets: 2. Validation and first results. *J. Geophys. Res.*, **100**, 1167–1197, <https://doi.org/10.1029/94JD02746>.
- , and R. A. Schiffer, 1999: Advances in understanding clouds from ISCCP. *Bull. Amer. Meteor. Soc.*, **80**, 2261–2287, [https://doi.org/10.1175/1520-0477\(1999\)080<2261:AIUCFI>2.0.CO;2](https://doi.org/10.1175/1520-0477(1999)080<2261:AIUCFI>2.0.CO;2).
- , and Coauthors, 1985: ISCCP cloud algorithm intercomparison. *J. Climate Appl. Meteor.*, **24**, 877–903, [https://doi.org/10.1175/1520-0450\(1985\)024<0887:ICAI>2.0.CO;2](https://doi.org/10.1175/1520-0450(1985)024<0887:ICAI>2.0.CO;2).
- Sassen, K., and Z. Wang, 2008: Classifying clouds around the globe with the CloudSat radar: 1 year of results. *Geophys. Res. Lett.*, **35**, L04805, <https://doi.org/10.1029/2007GL032591>.
- , and —, 2012: The clouds of the middle troposphere: Composition, radiative impact, and global distribution. *Surv. Geophys.*, **33**, 677–691, <https://doi.org/10.1007/s10712-011-9163-x>.
- , —, and D. Liu, 2008: Global distribution of cirrus clouds from CloudSat/Cloud-Aerosol Lidar and Infrared Pathfinder Satellite Observations (CALIPSO) measurements. *J. Geophys. Res.*, **113**, D00A12, <https://doi.org/10.1029/2008JD009972>.
- Shonk, J. K., R. J. Hogan, and J. Manners, 2012: Impact of improved representation of horizontal and vertical cloud structure in a climate model. *Climate Dyn.*, **38**, 2365–2376, <https://doi.org/10.1007/s00382-011-1174-2>.
- Stackhouse, P. W., Jr., S. K. Gupta, S. J. Cox, T. Zhang, J. C. Mikovert, and L. M. Hinkelman, 2011: The NASA/GEWEX surface radiation budget release 3.0: 24.5-year dataset. *GEWEX News*, No. 20 (1), International GEWEX Project Office, Silver Spring, MD, 10–12.
- Stephens, G. L., 2005: Cloud feedbacks in the climate system: A critical review. *J. Climate*, **18**, 237–273, <https://doi.org/10.1175/JCLI-3243.1>.
- , and P. J. Webster, 1981: Clouds and climate: Sensitivity of simple systems. *J. Atmos. Sci.*, **38**, 235–247, [https://doi.org/10.1175/1520-0469\(1981\)038<0235:CACSOS>2.0.CO;2](https://doi.org/10.1175/1520-0469(1981)038<0235:CACSOS>2.0.CO;2).
- , and T. J. Greenwald, 1991: The Earth's radiation budget and its relation to atmospheric hydrology 2: Observations of cloud effects. *J. Geophys. Res.*, **96**, 15 325–15 340, <https://doi.org/10.1029/91JD00972>.
- , and N. B. Wood, 2007: Properties of tropical convection observed by millimeter-wave radar systems. *Mon. Wea. Rev.*, **135**, 821–842, <https://doi.org/10.1175/MWR3321.1>.
- , and Coauthors, 2002: The CloudSat mission and the A-Train: A new dimension of space-based observations of clouds and precipitation. *Bull. Amer. Meteor. Soc.*, **83**, 1771–1790, <https://doi.org/10.1175/BAMS-83-12-1771>.
- , and Coauthors, 2012: An update on Earth's energy balance in light of the latest global observations. *Nat. Geosci.*, **5**, 691–696, <https://doi.org/10.1038/ngeo1580>.
- , M. Z. Hakuba, M. Hawcroft, J. M. Haywood, A. Behrangi, J. E. Kay, and P. J. Webster, 2016: The curious nature of the hemispheric symmetry of the earth's water and energy balances. *Curr. Climate Change Rep.*, **2**, 135–147, <https://doi.org/10.1007/s40641-016-0043-9>.
- , D. Winker, J. Pelon, C. Trepte, D. Vane, C. Yuhas, T. L'ecuyer, and M. Lebsock, 2018: *CloudSat and CALIPSO within the A-Train: Ten years of actively observing the Earth system*. *Bull. Amer. Meteor. Soc.*, **99**, 569–581, <https://doi.org/10.1175/BAMS-D-16-0324.1>.
- Su, H., and Coauthors, 2013: Diagnosis of regime-dependent cloud simulation errors in CMIP5 models using “A-Train” satellite observations and reanalysis data. *J. Geophys. Res.*, **118**, 2762–2780, <https://doi.org/10.1029/2012JD018575>.
- Su, W., A. Bodas-Salcedo, K.-M. Xu, and T. P. Charlock, 2010: Comparison of the tropical radiative flux and cloud radiative effect profiles in a climate model with Clouds and the Earth's Radiant Energy System (CERES) data. *J. Geophys. Res.*, **115**, D01105, <https://doi.org/10.1029/2009JD012490>.
- Tanelli, S., S. L. Durden, E. Im, K. S. Pak, D. G. Reinke, P. Partain, J. M. Haynes, and R. T. Marchand, 2008: CloudSat's cloud profiling radar after two years in orbit: Performance, calibration, and processing. *IEEE Trans. Geosci. Remote Sens.*, **46**, 3560–3573, <https://doi.org/10.1109/TGRS.2008.2002030>.
- Trenberth, K. E., J. T. Fasullo, and J. Kiehl, 2009: Earth's global energy budget. *Bull. Amer. Meteor. Soc.*, **90**, 311–324, <https://doi.org/10.1175/2008BAMS2634.1>.
- , —, and M. A. Balmaseda, 2014: Earth's energy imbalance. *J. Climate*, **27**, 3129–3144, <https://doi.org/10.1175/JCLI-D-13-00294.1>.
- Tselioudis, G., and C. Jakob, 2002: Evaluation of midlatitude cloud properties in a weather and a climate model: Dependence on dynamic regime and spatial resolution. *J. Geophys. Res.*, **107**, 4781, <https://doi.org/10.1029/2002JD002259>.
- Wang, Z., and K. Sassen, 2001: Cloud type and macrophysical property retrieval using multiple remote sensors. *J. Appl. Meteor.*, **40**, 1665–1682, [https://doi.org/10.1175/1520-0450\(2001\)040<1665:CTAMPR>2.0.CO;2](https://doi.org/10.1175/1520-0450(2001)040<1665:CTAMPR>2.0.CO;2).
- , D. Vane, G. Stephens, and D. Reinke, 2012: Level 2 combined radar and lidar cloud scenario classification product process description and interface control document. JPL Rep., 22 pp.
- Webb, M., C. Senior, S. Bony, and J.-J. Morcrette, 2001: Combining ERBE and ISCCP data to assess clouds in the Hadley Centre, ECMWF and LMD atmospheric climate models. *Climate Dyn.*, **17**, 905–922, <https://doi.org/10.1007/s003820100157>.
- Wielicki, B. A., B. R. Barkstrom, E. F. Harrison, R. B. Lee III, G. L. Smith, and J. E. Cooper, 1996: Clouds and the Earth's Radiant Energy System (CERES): An Earth observing system experiment. *Bull. Amer. Meteor. Soc.*, **77**, 853–868, [https://doi.org/10.1175/1520-0477\(1996\)077<0853:CATERE>2.0.CO;2](https://doi.org/10.1175/1520-0477(1996)077<0853:CATERE>2.0.CO;2).
- Wild, M., 2005: Solar radiation budgets in atmospheric model intercomparisons from a surface perspective. *Geophys. Res. Lett.*, **32**, L07704, <https://doi.org/10.1029/2005GL022421>.
- , 2008: Short-wave and long-wave surface radiation budgets in GCMs: A review based on the IPCC-AR4/CMIP3 models. *Tellus*, **60A**, 932–945, <https://doi.org/10.1111/j.1600-0870.2008.00342.x>.
- , A. Ohmura, H. Gilgen, J.-J. Morcrette, and A. Slingo, 2001: Evaluation of downward longwave radiation in general circulation models. *J. Climate*, **14**, 3227–3239, [https://doi.org/10.1175/1520-0442\(2001\)014<3227:EODLRI>2.0.CO;2](https://doi.org/10.1175/1520-0442(2001)014<3227:EODLRI>2.0.CO;2).

- , D. Folini, C. Schär, N. Loeb, E. G. Dutton, and G. König-Langlo, 2013: The global energy balance from a surface perspective. *Climate Dyn.*, **40**, 3107–3134, <https://doi.org/10.1007/s00382-012-1569-8>.
- Winker, D. M., W. H. Hunt, and M. J. McGill, 2007: Initial performance assessment of CALIOP. *Geophys. Res. Lett.*, **34**, L19803, <https://doi.org/10.1029/2007GL030135>.
- Wyant, M. C., C. S. Bretherton, J. T. Bacmeister, J. T. Kiehl, I. M. Held, M. Zhao, S. A. Klein, and B. J. Soden, 2006: A comparison of low-latitude cloud properties and their response to climate change in three AGCMs sorted into regimes using mid-tropospheric vertical velocity. *Climate Dyn.*, **27**, 261–279, <https://doi.org/10.1007/s00382-006-0138-4>.
- Xu, K.-M., T. Wong, B. A. Wielicki, L. Parker, and Z. A. Eitzen, 2005: Statistical analyses of satellite cloud object data from CERES. Part I: Methodology and preliminary results of the 1998 El Niño/2000 La Niña. *J. Climate*, **18**, 2497–2514, <https://doi.org/10.1175/JCLI3418.1>.
- , —, S. Dong, F. Chen, S. Kato, and P. C. Taylor, 2016: Cloud object analysis of CERES *Aqua* observations of tropical and subtropical cloud regimes: Four-year climatology. *J. Climate*, **29**, 1617–1638, <https://doi.org/10.1175/JCLI-D-14-00836.1>.
- Zhang, D., Z. Wang, and D. Liu, 2010: A global view of mid-level liquid-layer topped stratiform cloud distribution and phase partition from CALIPSO and CloudSat measurements. *J. Geophys. Res.*, **115**, D00H13, <https://doi.org/10.1029/2009JD012143>.
- Zhang, M., and Coauthors, 2005: Comparing clouds and their seasonal variations in 10 atmospheric general circulation models with satellite measurements. *J. Geophys. Res.*, **110**, D15S02, <https://doi.org/10.1029/2004JD005021>.
- Zhang, T., P. W. Stackhouse Jr., S. K. Gupta, S. J. Cox, J. C. Mikovitz, and L. M. Hinkelman, 2013: The validation of the GEWEX SRB surface shortwave flux data products using BSRN measurements: A systematic quality control, production and application approach. *J. Quant. Spectrosc. Radiat. Transf.*, **122**, 127–140, <https://doi.org/10.1016/j.jqsrt.2012.10.004>.
- Zhang, Y.-C., W. B. Rossow, and A. A. Lacis, 1995: Calculation of surface and top of atmosphere radiative fluxes from physical quantities based on ISCCP data sets: 1. Method and sensitivity to input data uncertainties. *J. Geophys. Res.*, **100**, 1149–1165, <https://doi.org/10.1029/94JD02747>.
- , —, —, V. Oinas, and M. I. Mishchenko, 2004: Calculation of radiative fluxes from the surface to top of atmosphere based on ISCCP and other global data sets: Refinements of the radiative transfer model and the input data. *J. Geophys. Res.*, **109**, D19105, <https://doi.org/10.1029/2003JD004457>.